1 **Large Spatiotemporal Variability in Aerosol Properties over Central Argentina during the**
2 **CACTI Field Campaign**

3 Jerome D. Fast[1], Adam C. Varble[1], Fan Mei[1], Mikhail Pekour[1], Jason Tomlinson[1], Alla
4 Zelenyuk[1], Art J. Sedlacek III[2], Maria Zawadowicz[2], and Louisa Emmons[3]

5 [1]Pacific Northwest National Laboratory, Richland, Washington, United States
6 [2]Brookhaven National Laboratory, Upton, New York, United States
7 [3]NSF National Center for Atmospheric Research, Boulder, Colorado, United States

8 *Correspondence to:* Jerome D. Fast (jerome.fast@pnnl.gov)

9 **Abstract**

10 Few field campaigns with extensive aerosol measurements have been conducted over continental areas in
11 the southern hemisphere. To address this data gap and better understand the interactions of convective
12 clouds and the surrounding environment, extensive in situ and remote sensing measurements were
13 collected during the Cloud, Aerosol, and Complex Terrain Interactions (CACTI) field campaign
14 conducted between October 2018 and April 2019 over the Sierras de Córdoba range of central Argentina.
15 This study describes measurements of aerosol number, size, composition, mixing state, and cloud
16 condensation nuclei (CCN) collected at the ground and from a research aircraft during seven weeks of the
17 campaign. Large spatial and multi-day variations in aerosol number, size, composition, and CCN were
18 observed due to transport from upwind sources controlled by mesoscale to synoptic-scale meteorological
19 conditions. Large vertical wind shears, back trajectories, single particle measurements, and chemical
20 transport model predictions indicate that different types of emissions and source regions, including
21 biogenic emissions and biomass burning from the Amazon and anthropogenic emissions from Chile and
22 eastern Argentina, contribute to aerosols observed during CACTI. Repeated aircraft measurements near
23 the boundary layer top reveal strong spatial and temporal variations in CCN and demonstrate that
24 understanding the complex co-variability of aerosol properties and clouds is critical to quantify the impact
25 of aerosol-cloud interactions. In addition to quantifying aerosol properties in this data-sparse region, these
26 measurements will be valuable to evaluate predictions over the mid latitudes of South America and
27 improve parameterized aerosol processes in local, regional, and global models.

28 **1. Introduction**

29 Earth system models (ESMs), high-resolution models, and observations are key tools for improving our
30 understanding of the natural and human-influenced atmospheric processes affecting Earth's climate.
31 Despite recent scientific advances, models still contain biases arising from knowledge gaps and imperfect
32 parameterizations of important atmospheric processes. The impacts of these biases are multifaceted, but
33 they make important contributions to uncertainties in the net change of the Earth system energy balance
34 between preindustrial and present-day periods. Much of this uncertainty has been attributed to current
35 understanding and/or representation of aerosol–cloud interaction (ACI) processes and the magnitude of
36 this uncertainty among ESM predictions has remained unchanged for Intergovernmental Panel on Climate
37 Change (IPCC) assessments since 1995 (Seinfeld et al., 2016; Carslaw et al., 2018).

38 Aerosols are known to perturb cloud hydrometeors, albedo, growth, dissipation, lifetime, and
39 precipitation (Twomey 1974; Albrecht 1989; Rosenfeld et al., 2014) that subsequently influence climate
40 over long time scales. ACI processes depend on the co-variability of aerosol and cloud properties. While
41 the impact of aerosols on shallow marine stratocumulus has been studied extensively (e.g., Twohy et al.,
42 2005; Wood et al., 2011; Feingold et al., 2024), there are few measurements that characterize the
43 spatiotemporal variability of key aerosol properties in the presence of convective cloud populations that
44 can be observed routinely by satellites. One challenge for models is that the spatiotemporal variability of
45 aerosols and convective clouds is often subgrid-scale (e.g. Fast et al., 2022). While models often contain
46 parameterizations of subgrid-scale variability for certain cloud types they usually assume aerosols are
47 constant within a grid cell which could lead to erroneous estimates of the impact of ACI. In addition to

48   model resolution of intersecting aerosol and cloud properties, there are complex ACI pathways for
49   convective clouds that are still highly uncertain (Fan et al., 2016; Varble et al., 2023) for many reasons.

50   Aircraft in situ and remote sensing data provide key spatiotemporal measurements of aerosol properties
51   needed to develop an improved understanding of aerosol processes and evaluate and improve models.
52   Aircraft campaigns are usually relatively short (i.e. a few weeks or less) and do not have the global
53   coverage of satellite and ground measurements. Most aircraft field campaigns that include aerosol
54   measurements have been conducted over the northern hemisphere (Reddington et al., 2017; Watson-Parris
55   et al., 2019). Field campaigns in the southern hemisphere have been conducted in the tropics, such as the
56   Green Ocean Amazon Experiment, (GoAmazon, Martin et al., 2017) or over the southern hemisphere
57   ocean, such as the VAMOS Ocean-Cloud-Atmosphere-Land Study Regional Experiment (VOCALS-Rex,
58   Wood et al., 2011), Southern Ocean Clouds, Radiation, Aerosol Transport Experimental Study
59   (SOCRATES, McFarquhar et al., 2021), and the combined CLouds–Aerosol–Radiation Interaction and
60   Forcing for Year 2017 (CLARIFY-2017), ObseRvations of Aerosols above CLouds and their
61   intEractionS (ORACLES), and Layered Atlantic Smoke and Interactions with Clouds (LASIC)
62   experiments conducted over the southeast Atlantic Ocean (Barrett et al., 2022). Global aircraft campaigns,
63   such as the HIAPER Pole-to-Pole Observations (HIPPO, Wofsy et al., 2011) and the Atmospheric
64   Tomography Mission (AToM, Brock et al., 2019) obtained snapshots of aerosol measurements over both
65   hemispheres, primarily over the ocean. Few aerosol field campaigns with extensive aerosol
66   measurements, however, have been conducted over subtropical and midlatitude continental areas in the
67   southern hemisphere.

68   To address this data gap and better understand the interactions of convective clouds and the surrounding
69   environment, extensive in situ and remote sensing measurements were collected during the Cloud,
70   Aerosol, and Complex Terrain Interactions (CACTI) field campaign conducted between October 2018
71   and April 2019 over the Sierras de Córdoba range of central Argentina (Varble et al., 2021). The U.S.
72   Department of Energy's Atmospheric Radiation Measurement (ARM) mobile facility (AMF, Mather and
73   Voyles, 2013) and G-1 research aircraft (Schmid et al., 2014) were deployed during CACTI. The field
74   campaign was designed to address science questions related to how orographic convective clouds interact
75   with and depend on environmental conditions, thermodynamics, aerosols, and surface properties. CACTI
76   occurred at the same time and in the same region as the National Science Foundation (NSF)-led Remote
77   Sensing of Electrification, Lightning, and Mesoscale/Microscale Processes with Adaptive Ground
78   Observations (RELAMPAGO) field campaign (Nesbitt et al., 2021). Observations from CACTI have
79   been used to characterize the range of deep convective cloud life cycles and their relationships with
80   ambient environments (Feng et al., 2022, 2023), determine the environmental conditions favorable for
81   deep convection initiation (Marquis et al., 2021, 2023; Nelson et al., 2022), identify factors affecting rain
82   rates in warm clouds (Borque et al., 2022), examine the relationship between depth of convective cores
83   and aerosol concentrations (Veals et al., 2022), evaluate the ability of kilometer scale simulations to
84   represent the characteristics of mesoscale convective systems (Zhang et al., 2021), and determine the
85   influence of the South American low-level jet on the convective environment (Sasaki et al., 2023).

86   In contrast with the previous studies that focus on clouds, this paper describes measurements of aerosol
87   number, size, composition, mixing state, and cloud condensation nuclei (CCN) collected by the AMF and
88   G-1 platforms during the CACTI campaign. It is important to understand the spatiotemporal variation of
89   aerosol properties before assessing how those properties influence convective clouds forming along the
90   Sierras de Córdoba (SDC) range. CACTI measurements are analyzed to demonstrate the multi-day and
91   diurnal variations in aerosol properties at the ground as well as the vertical and horizontal variations of
92   aerosols aloft. As will be shown later, large multi-day variations in aerosol number, size, composition,
93   and CCN was observed due to regional to long-range transport from upwind sources that is controlled by
94   mesoscale to synoptic-scale meteorological processes. Since repeated aircraft measurements near the
95   boundary layer top reveal strong spatial and temporal variations in CCN, inferring the impact of aerosols
96   on convective clouds over the region will be challenging.

2. Measurements and Models

2.1 Ground measurements

A wide range of continuous meteorological, radiation, and aerosol measurements were collected at the ground by the ARM mobile facility (AMF, Mather and Voyles, 2013) during CACTI between 15 October 2018 and 30 April 2019. As shown in Fig. 1a, the AMF was located along the eastern slope of the SDC at an elevation of 1141 m MSL. The mountains along the continuous ~300-km long north-south crest of the SDC are as high as ~2790 m MSL. About 100 km northeast of the AMF site is Córdoba, the largest city in the region with an urban population of ~2.1 million. Rio Cuarto, ~130 km southeast of the AMF site, is the second largest city in the region with a population of nearly 180,000. Alta Gracia and Rio Tercero are ~60 km to the northeast and east, respectively, each having a population of ~45,000, while Villa Carlos Paz 80 km to the north has a population of 75,000. Villa Dolores, 50 km to the west on the other side of the SDC crest, has a population of 30,000. The SDC and the lower slopes surrounding mountain range, however, are much less populated with no more than a handful of towns having populations near 10,000.
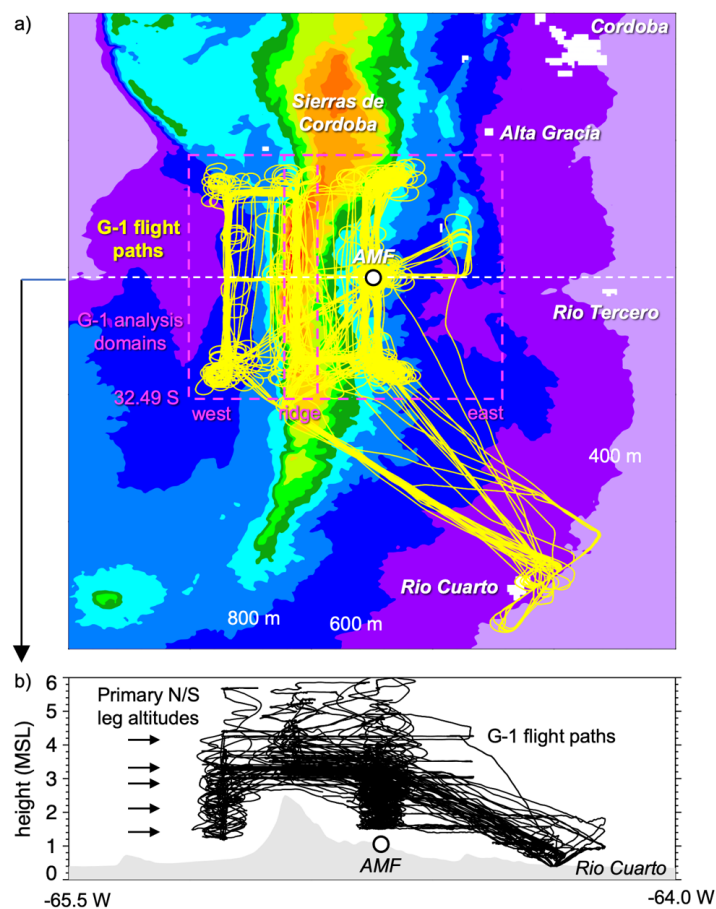
Figure 1.   a) Topography of Sierras de Córdoba and the location of AMF ground site and horizontal G-1 flight paths and b) west-east cross section of topography at the AMF latitude and the altitude of the G-1 flight paths. In a), the white cells denote urban areas and magenta dashed lines denote three analysis domains for the G-1 data.

115

116 Near-surface winds (Kyrouac et al., 2018) during the CACTI campaign were predominately from the
117 northeast; otherwise, the winds were usually from the east to southeast (Fig. S1a). At about 2.5 km MSL
118 which is often within the afternoon convective boundary layer, winds obtained from the radiosondes (3 –
119 5 per day; Keeler et al. 2018) were mostly from the north to northeast (Fig. S1b). Winds were usually
120 from the northwest in the transition zone between the daytime convective boundary layer and free
121 troposphere at 3 km MSL (Fig. S1c) and were predominantly from the west at higher altitudes such those
122 at 4.5 km MSL (Fig. S1d). The lower frequency of easterly winds suggests that aerosols originating from
123 the most populated areas of Argentina near Buenos Aires are not often directly transported to the AMF
124 site. However, they may be transported to the site by more complex circulations. The common directional
125 vertical wind shear indicates that aerosols measured at the AMF site could originate from different
126 locations at the same time, as will be discussed later.

127 The AMF aerosol measurements used in this study are listed in Table 1. Measurements of aerosol optical
128 depth at five wavelengths, total aerosol number concentration, aerosol chemical composition, aerosol size
129 distribution, and CCN concentrations at six supersaturations were collected during the 6.5-month period.
130 Measurements of scattering (nephelometer) and absorption (particle soot absorption photometer) by
131 aerosols were also collected but are not used in this study. Aerosol optical depth at five wavelengths is
132 derived from the multifilter rotating shadowband radiometer (MFRSR) during the day when the sky is
133 relatively free of clouds (Koontz et al. 2018a). Two particle condensation counters (CPC) obtained total
134 aerosol number concentration for particle diameters greater than 3 (Koontz et al. 2018b) and 10 nm
135 (Koontz et al. 2018c). The aerosol chemical speciation monitor (ACSM, Ng et al. 2011) measures bulk
136 non-refractory organic matter, sulfate, nitrate, ammonium, and chloride for particle sizes less than 1 μm
137 (Zawadowicz et al., 2018). Refractory black carbon (rBC) concentrations and size distributions are
138 measured by a single particle soot photometer (SP2, Schwarz et al., 2006). The scanning mobility particle
139 sizer (SMPS) obtained aerosol concentration for 106 size bins ranging from 10.9 to 495.8 nm (Kuang et
140 al., 2018). The ultrahigh sensitivity aerosol spectrometer (UHSAS) collected aerosol concentrations for
141 299 size bins between 55.81 and 985.5 nm (Uin et al., 2018). The SMPS and UHSAS size distribution
142 was combined to obtain a single aerosol size distribution, with the SMPS and UHSAS values merged
143 around diameters of 260 nm. The first column of the CCN counter cycles through six supersaturations
144 with measurements at each supersaturation lasting~10 min (Koontz at al. 2018d) and the second column
145 continuously samples CCN at 0.4% supersaturation (Koontz et al., 2018e). Trace gas measurements
146 consisted of carbon monoxide (CO; Koontz et al., 2018f) and ozone (O_3, Springston et al., 2018) and did
147 not include aerosol precursor gas-phase species. Additional details on these instruments and a description
148 of the meteorological and radiation measurements are presented in Varble et al. (2019, 2021).

149 Table 1. Aerosol measurements, instruments, and sampling rates between 15 October 2018 and 30 April
150 2019 at the AMF site.

Measurement	Instrumentation	Sampling Rate
aerosol optical depth	multifilter rotating shadowband radiometer (MFRSR) at 415, 500, 615, 673, 870 nm	20 s
aerosol number concentration	ultrafine (> 3 nm) and fine (> 10 nm) condensation particle counters (CPC)	1 s
aerosol chemical composition	aerosol chemical speciation monitor (ACSM), single-particle soot photometer (SP2)	~30 min, ~ 1 min
aerosol size distribution	ultrahigh sensitivity aerosol spectrometer (UHSAS), scanning mobility particle sizer (SMPS), best estimate aerosol size distribution (BEASD)	1 s, 64 s interpolated to 1 s 1 s
cloud condensation nuclei (CCN) concentration	dual column CCN counter (0.1, 0.2, 0.4, 0.6, 0.8, 1% supersaturation)	1 s
trace-gas concentrations	O_3, CO monitoring systems	1 s

151   2.2 Aircraft measurements

152   The G-1 aircraft (Schmid et al. 2014) collected a wide range of meteorological, radiation, trace gas, and
153   aerosol measurements around the AMF site over 79.4 h on 22 days between 4 November and 8 December
154   2018. Flight durations were usually ~4 h, although flight durations on a few days were closer to ~2 h. All
155   flights were conducted between 0915 and 1715 LT and flights were either during the morning, mid-day,
156   or afternoon. All the flight paths that originated at the Rio Cuarto airport where aircraft operations were
157   based are depicted in Fig. 1a. Most of the science flight time was spent along north-south transects at
158   constant altitudes over the AMF site, over the crest of the mountain range, and over the western slope of
159   the of the SDC. The constant altitude flight legs were conducted below ~4 km MSL although some
160   profiles were made up to 6 km MSL as shown in Fig. 1b. These aircraft measurements describe the
161   spatiotemporal variability of aerosol properties in the boundary layer and free troposphere over the same
162   region where deep convection frequently forms (Feng et al., 2022).

163   One of the objectives of CACTI was to determine how environmental conditions (including aerosol
164   properties) influence convective cloud life cycles and how those convective clouds in turn alter aerosol
165   properties; therefore, many of the constant altitude flight legs were at or just below cloud base. Cloud
166   sampling was usually done within shallow cumulus or cumulus congestus, most frequently observed to
167   form along the crest of the SDC. Three out of the 22 G-1 flights were conducted on clear-sky days to
168   sample boundary layer and lower free troposphere aerosol properties.

169   Profiles of aerosol properties in the vicinity of the AMF site were likely influenced by vertical wind
170   shears, boundary layer mixing, convective updrafts and downdrafts, and cloud processing. However, few
171   true profiles through the depth of the boundary layer and lower free troposphere were made since the
172   flight paths usually consisted of constant altitude legs connected by short vertical ascents/descents
173   between those legs. As described later, the aircraft sampling strategy combined with the large
174   spatiotemporal variability of aerosol properties complicates the interpretation of vertical profiles of
175   aerosol properties within a short time window.

176   Table 2 lists the G-1 aircraft aerosol measurements used in this study. Two CPC instruments, with 3 and
177   10 nm lower cutoffs, were deployed on the aircraft to provide the same type of total aerosol number
178   concentrations as the ground site (Koontz et al. 2018g,h). The miniSPLAT (Zelenyuk et al., 2015)
179   instrument was deployed to measure the chemical composition of thousands of individual particles. While
180   miniSPLAT does not produce bulk concentrations of aerosol composition like a high-resolution time-of-
181   flight aerosol mass spectrometer (HR-ToF-AMS, DeCarlo et al. 2006), it does provide information on
182   size and composition of individual aerosol particles, which determine aerosol activation into cloud
183   droplets (e.g., Saliba et al., 2023). miniSPLAT measures the size, nonrefractory composition, and
184   refractory composition (e.g., soot, sea salt, dust) of several hundreds of individual particles per minute to

185   Table 2.   G-1 aircraft aerosol measurements, instrumentation, and sampling rate between 4 November
186   and 8 December 2018.

Measurement	Instrumentation	Sampling Rate
aerosol number concentration	ultrafine (> 3 nm) and fine (> 10 nm) condensation particle counters (CPC)	1 s
aerosol chemical composition	single-particle mass spectrometer (miniSPLAT), derived particle class information	0.05 s 300 s
aerosol size distribution	scanning mobility particle sizer (SMPS), ultrahigh sensitivity aerosol spectrometer (UHSAS), cloud aerosol spectrometer (CAS), fast cloud droplet probe (FCDP), best estimate aerosol size distribution (BEASD)	1 s
cloud condensation nuclei (CCN) concentration	dual column CCN counter (0.2, 0.5% supersaturation)	1 s
trace-gas concentrations	O_3, CO, SO_2 monitoring systems	1 s

187 obtain information on aerosol mixing state. The single particle mass spectra were classified into hundreds
188 of clusters, which for simplicity have been subsequently combined into 14 distinct, physically
189 meaningful, aerosol types or classes (Zelenyuk et al. 2015). Aerosol size distribution was obtained from
190 SMPS (Mei and Pekour, 2018), UHSAS (Tomlinson, 2018), passive cavity aerosol spectrometer (PCASP;
191 Marinovici and Tomlinson, 2018), cloud aerosol spectrometer (CAS; Cromwell et al., 2018), and fast
192 cloud droplet probe (FCDP; Mei et al., 2018) instruments. CAS and FCDP are usually used to obtain
193 droplet size distribution, but they also provide coarse mode aerosol number concentration outside of
194 clouds with additional data processing. The merged aerosol size distribution ARM data product (Pekour
195 and Ermold, 2023) combines data from these four instruments to produce 35 size bins from 15 nm to 9.69
196 μm and is used for our analyses of aircraft aerosol size distributions. In contrast to the ground CCN
197 instrument, continuous measurements of CCN were obtained at 0.2 and 0.5% supersaturations (Koontz et
198 al., 2018i,j). Trace gas measurements included sulfur dioxide (SO_2; Burk et al., 2018a) in addition to CO
199 (Burk and Ermold, 2018) and O_3 (Burk et al., 2018b). The SO_2 monitor was able to detect large sulfur
200 dioxide plumes greater than ~1 ppb. SO_2 data below ~1 ppb was quite noisy and cannot be used to
201 examine spatial variability at ppt levels. As with the ground instrumentation, there were no measurements
202 of trace gas aerosol precursors. The 1-s sampling rate combined with G-1 flight speed of 100 m s^{-1} results
203 in aerosol measurements over 100 m distances.

204 2.3 CAM-Chem description

205 The Community Atmosphere Model with chemistry (CAM-chem), a component of the Community Earth
206 System Model (Danabasoglu et al., 2020) is used to illustrate transport pathways of smoke during
207 CACTI. This version of the model uses the MOZART-TS1 chemical mechanism (Emmons et al. 2020)
208 and the Modal Aerosol Model version 4 (MAM4, Liu et al., 2016; Tilmes et al., 2019). The
209 meteorological fields are nudged to the Modern-Era Retrospective analysis for Research and
210 Applications, Version 2 (MERRA-2) meteorological analyses. Simulation output with a horizontal grid
211 spacing of 1.25 x 0.94 degrees is available (Tilmes et al., 2022) at 6-hour intervals from 2001 – 2020.

212 **3. Results**

213 3.1 Multi-day and diurnal variability of ground aerosol measurements

214 Even though the SDC is not heavily populated, Fig 2a shows large multi-day variations in aerosol mass
215 for particles less than 1 μm in diameter (PM1) from the ACSM and black carbon from the SP2. For
216 example, PM1 concentrations were as high as 15.8 μg m^{-3} on November 2 and close to zero on days with
217 rain (October 25-26, November 11-12, 26-27). The highest PM1 concentrations occurred between the rain
218 events on October 25-26 and November 11-12 (period A, Figs. S2a and S2b). Between the November 11-
219 12 and 26-27 rain events (period B), the lowest PM1 concentrations occurred. After November 27 (period
220 C), PM1 concentrations increase somewhat but are still lower than during period A. In addition to wet
221 scavenging, the large day-to-day variability is likely due to interactions of synoptic and terrain-induced
222 circulations that transport biogenic, anthropogenic, and biomass burning aerosols from different source
223 regions to the site. The temporal variation of PM1 is somewhat correlated (r = 0.56 and 0.52 for 415 and
224 500 nm, respectively) with AOD (Fig. S3a), suggesting that aerosols in the boundary layer contribute to a
225 large fraction of the column integrated extinction. Note that AOD measurements are missing on 43% of
226 the daytime periods due to partly to mostly cloudy conditions as indicated by the KAZR-ARSCL (Ka-
227 band ARM Zenith Radar, Active Remote Sensing of CLouds) ARM product (Johnson et al., 2018; Fig.
228 S3b). Relatively high and low PM1 concentrations and AOD are often associated with northerly and
229 southerly winds, respectively, as will be shown later. While multiday trends in PM1 and AOD are similar,
230 they differ over several hours on some days (e.g., November 23) indicating the presence of aerosol layers
231 in the free troposphere that significantly contribute to column extinction.

232 Figure 2b shows that most of the PM1 mass is comprised of organic matter (OM, 53% on average) and
233 sulfate (SO_4, 29% on average). The relative contribution of OM is larger on days with relatively high
234 PM1 concentrations, while the relative contribution of SO_4 is usually larger on days when PM1

235 concentrations are less than 1 μg m^{-3}. Nitrate (NO$_3$) and ammonium (NH$_4$) each comprise 8% of the PM1
236 concentrations on average between October 23 and December 15. While the fraction of NH$_4$ does not
237 vary significantly during the campaign, the fraction of NO$_3$ varies substantially. Though NO$_3$ is very
238 small on many days, it contributes to over 20% of the total mass during 6% of this measurement period.
239 OM, SO$_4$, NH$_4$, and NO$_3$ concentrations all exhibited similar variations as PM1 among periods A, B, and
240 C (Figs. S2a - S2e).

241
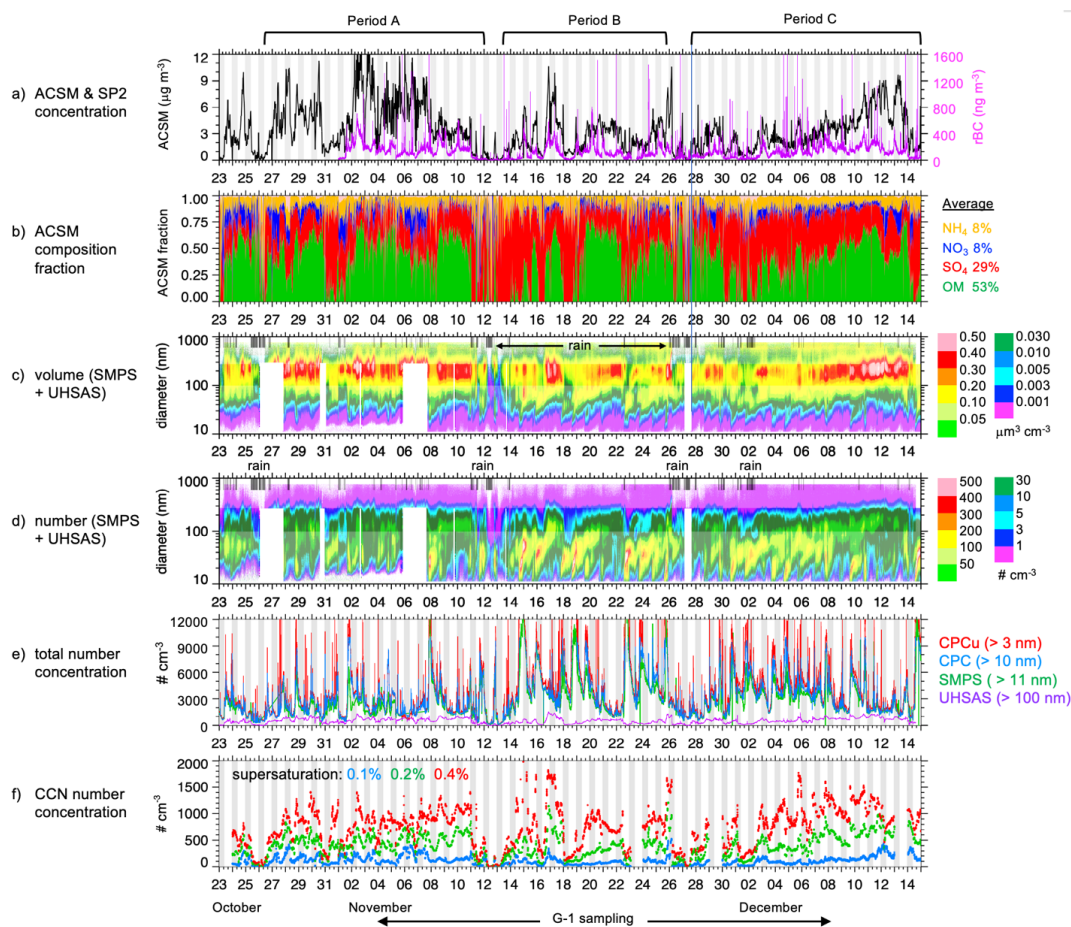
Figure 2.   Time series of a) PM1 and rBC concentration, b) ACSM composition fraction, c) aerosol
242
243   volume distribution, d) aerosol number distribution, e) total number concentration, and f)
244   CCN concentration at three supersaturations, focusing on G-1 flights during the first two
245   months of CACTI.

246 Temporal variations in the volume size distribution (Fig. 2c) are consistent with the variability in PM1,
247 with volume decreasing dramatically during rain events. Outside of rain events, peak aerosol volume
248 usually occurs between 200 and 300 nm. The 25th to 75th percentiles of accumulation mode particles (>
249 100 nm) are the largest during periods A and C and the lowest during period B (Fig. S2f) consistent with
250 the variations in PM1 from the ACSM. Nevertheless, there are a few times during period B with the
251 highest accumulation mode number concentrations as indicated by the largest 95th percentile. Temporal
252 variations in aerosol number distributions (Fig. 2d) and total aerosol number concentrations (Fig. 2e)

253   reveal that new particle formation (NPF) events occur on many days that produce large numbers of
254   ultrafine particles (UFP, diameter < 50 nm). While rain removes a large fraction of accumulation mode
255   particles, smaller particles are not removed entirely by wet scavenging. In addition to differences in the
256   meteorology and trace gas precursors between the rain events, NPF and growth is mostly likely controlled
257   by the presence or absence of accumulation mode aerosols. Since gas-phase aerosol precursors
258   preferentially condense on the largest particles, the higher PM1 concentrations during period A
259   suppresses the formation and growth of UFP (Fig. S2g). Conversely, the lower PM1 concentrations
260   during period B permit more particles to form and grow by condensation of trace gas precursors. While
261   NPF events resume a few days after the rain on November 26 and 27, accumulation mode aerosols and
262   PM1 concentrations slowly increase after December 6 and suppress the formation and growth of UFP.
263   Thus, UFP and Aiken mode number concentrations during period C are somewhat lower than during
264   period B but higher than during period A.

265   CCN is a function of aerosol number, size, and hygroscopicity (Kohler, 1936; Petters and Kriendenweis,
266   2007). As with PM1 and accumulation mode aerosols, CCN concentrations decrease dramatically during
267   rain events (Fig. 2f). The temporal variations in CCN are similar to variations in number concentrations of
268   particles larger than 100 nm with a correlation coefficient (r) of 0.68, 0.88, and 0.86 for supersaturations
269   0.1, 0.2, and 0.4%, respectively. Therefore, differences in CCN concentrations (Figs. S4a) among the
270   three periods are similar to those from the accumulation mode aerosols (Fig. S2e); however, the 95th
271   percentile for CCN at 0.4% supersaturation is the highest during period B because particles with smaller
272   diameters (usually with higher concentrations) can activate. The ARM CCNKAPPA product (Kulkarni et
273   al., 2018), that combines Kohler theory with CCN and SMPS measurements, is used to examine the
274   critical diameter for activation and aerosol hygroscopicity (kappa, κ) between October 23 and December
275   15. As expected, critical diameters for activations decrease with increasing supersaturation. The median
276   critical diameters for 0.1, 0.2, and 0.4% supersaturation are, 195 to 210, 118 to 126, and 76 to 82 nm,
277   respectively (Fig. S4b); however, the interquartile variations among periods A, B, and C are usually small
278   (less than 7%). Hygroscopicity is also relatively low and invariant during the campaign period (Fig. S4c),
279   with median values ranging from 0.19 to 0.29. As indicated by the 95th percentiles, hydrophilic aerosols
280   occurred most often during period B followed by periods A and C. Determining the relative importance of
281   aerosol number, size, hygroscopicity, and mixing state factors on the temporal variations in CCN seen in
282   Fig. 2f will require a closure study (e.g. Kulkarni et al., 2023).

283   Figure 3a shows the average diurnal variations in aerosol composition, which reflect the impact of local
284   processes such as boundary layer mixing and photochemistry. SO_4 and NH_4 have little diurnal variability
285   during this seven-week period, suggesting multi-day transport may be the dominate process influencing
286   those concentrations over the AMF site. NO_3 has peak concentrations around sunrise that are twice as
287   high (0.4 µg m^{-3}) as those during the late afternoon (0.2 µg m^{-3}). This diurnal variability is likely due to
288   temperature dependent condensation/evaporation processes because the lowest temperatures occur at
289   sunrise and NO_3 tends to evaporate during warmer temperatures. Peak OM concentrations usually occur
290   during the afternoon, probably due to secondary organic aerosol (SOA) formation that depends on a wide
291   range of photochemical processes. The net increase in surface OM suggests that photochemistry and/or
292   entrainment of higher OM from the free troposphere more than compensates for the effects of growing
293   boundary layer dilution. The peak rBC concentration at night is more difficult to explain since there are
294   no local emissions of black carbon in the vicinity of the AMF site. Since rBC is chemically inert and can
295   be treated as a passive tracer, the diurnal variability is due to the combination of horizontal transport and
296   the effects of boundary layer mixing.

297   Ultrafine particle number concentrations from the SMPS (Fig. 3b) show maximum concentrations
298   occurring during the late afternoon at 20 UTC (17 LT). The diurnal variations in the UHSAS (Fig. 3c)
299   also indicate modest concentration increases during the later afternoon for particle diameters greater than
300   100 nm; however, there is no diurnal variability for particle diameters greater than 200 nm. This indicates
301   that most of the diurnal variability in aerosol number is driven by ultrafine and Aiken mode aerosols.

302   Since NPF events vary during the sampling period (Fig. 2d), we divide the diurnal variability in aerosol
303   number concentration into 19 days with concentrations always lower than 4000 cm^{-3} ("low-UFP"), 11
304   days (1 during period A, 6 during period B, 4 during period C) with number concentrations greater than
305   8000 cm^{-3} for at least one hour ("high-UFP"), and the 24 remaining days that fall in between the low-UFP
306   and high-UFP days. The high-UFP days exhibit the largest diurnal variability, the low-UFP days exhibit
307   no diurnal variability, and the remaining 24 days have modest diurnal variability that is closer to the
308   average over the entire period.

b) – f)
black = all days, 23 October - 15 December
blue = low UPF days (SMPS always < 4000 cm^{-3}): Oct. 23, 24, 25, 26, 29, 30; Nov. 3, 4, 5, 6, 9, 13, 21, 26, 27, 28; Dec. 6, 11, 12
red = high UPF days (SMPS > 8000 cm^{-3} or 1 h or more): Nov. 7, 14, 15, 16, 18, 22, 25, 29, 30; Dec. 7, 14
green = remaining 24 days
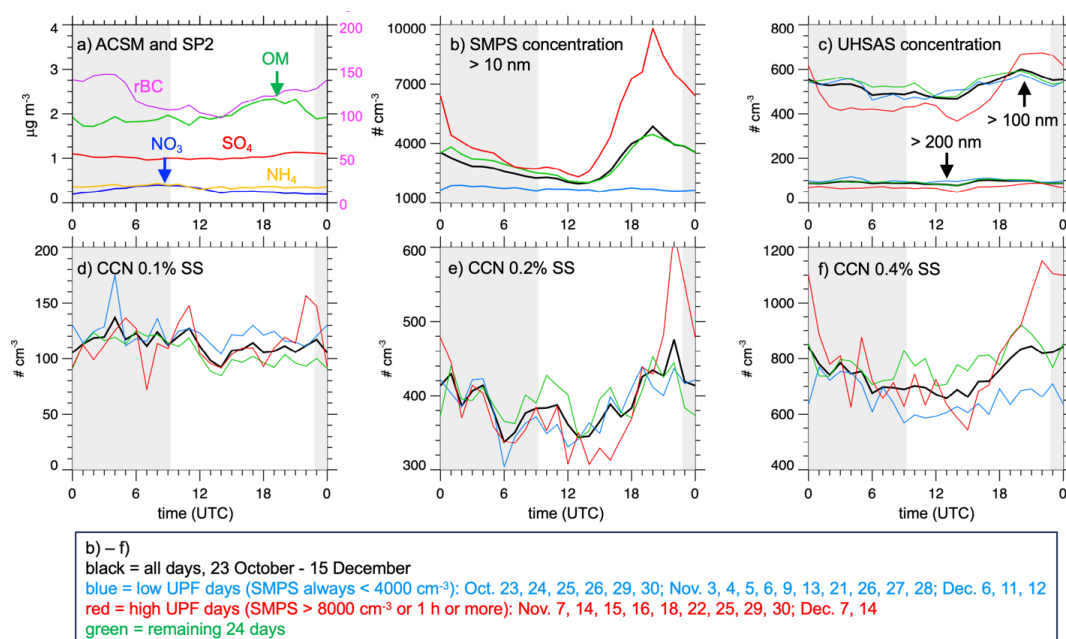
309

310   Figure 3.   Diurnal variability in a) aerosol composition, b) aerosol number concentration from SMPS, c)
311   aerosol number concentration from UHSAS, and CCN at d) 0.1%, e) 0.2%, and f) 0.4%
312   supersaturation.

313   The diurnal variations in CCN shown in Figs. 3d – 3f are closely related to the diurnal variability in
314   aerosol number. Both particles with diameters greater than 200 nm and CCN at 0.1% supersaturation
315   exhibited no diurnal variability (Fig. 3c and 3d), Smaller particles start to activate at 0.2% supersaturation
316   (Fig. 3e); therefore, CCN at this supersaturation exhibits a modest diurnal variation on average with
317   afternoon concentrations ~28% higher than earlier in the day. However, CCN concentrations during the
318   late afternoon on high UFP days are twice as high as those around 15 UTC (12 LT). Finally, particles
319   smaller than 100 nm start to activate at CCN at 0.4% supersaturation so that CCN concentrations at this
320   supersaturation (Fig. 3f) are about double those at 0.2% supersaturation with a similar late afternoon peak.
321   Note that for both 0.2 and 0.4% supersaturations, peak CCN concentrations on high UFP days occur ~2 h
322   later in the day and closer to sunset than aerosol number concentrations. This suggests growth in the
323   aerosol size distribution during the day influences CCN, consistent with the daily growth seen in Fig. 2d.

324   Figure 3c also shows that concentrations of particles with diameters greater than 200 nm are higher on
325   low-UFP days and conversely high-UFP days tend to have lower concentrations of larger particles.
326   Figures 4a and 4b illustrate the average aerosol number and volume size distribution for 23 October to 15
327   December along with the averages for the low-UFP and high-UFP days. The differences in the number
328   and volume distribution for particle diameters < 100 nm reflect the definition of these days and are

329 consistent with the differences in CCN among the three supersaturations. Peak number concentrations for
330 high-UFP days occur between 30 – 40 nm, while those on low-UFP days occur between 50 – 60 nm. In
331 addition, high-UFP days have lower concentrations for particle diameters between 150 – 600 nm, likely
332 reflecting the time between days to grow particles from UFP to accumulation mode size as indicated in
333 Fig. 2d. Differences in the aerosol size distribution leads to differences in the critical particle diameter for
334 CCN activation, which are largest for 0.4% supersaturation. The average aerosol number and volume size
335 distributions for periods A, B, and C are shown in Figs. 4c and 4d. Periods A and B have the lowest and
336 highest average UFP concentrations, respectively, since period B also contains the most high-UFP days.
337 Conversely, periods A and B have the highest and lowest accumulation mode concentrations,
338 respectively. The average aerosol size distribution for period C is between those for periods A and B. and
339 similar to the average size distribution between the whole October 23 and December 15 period in Figs. 4a
340 and 4b. As expected, the rainy days at the AMF site have the lowest aerosol concentrations for all particle
341 sizes.

342
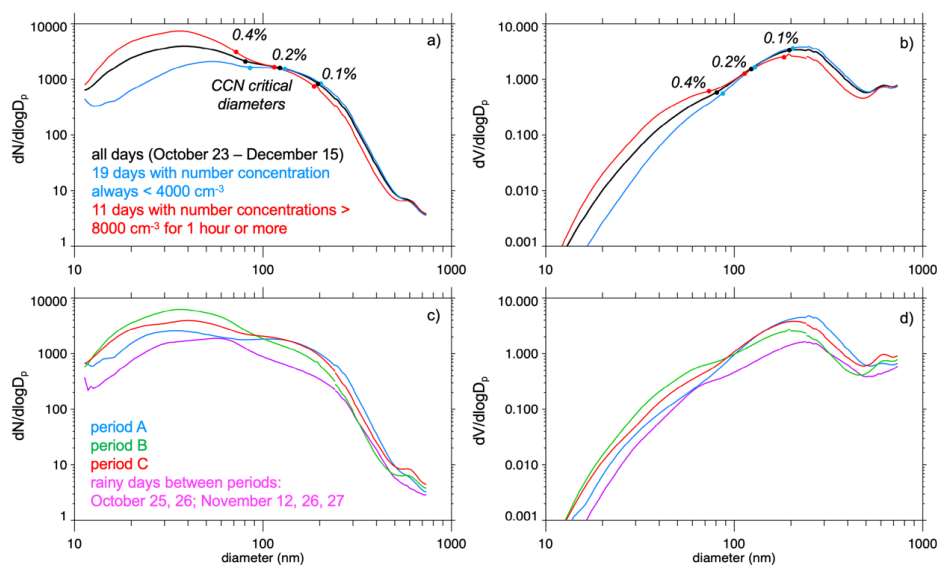
Figure 4.   Average size distributions at the ground site between 23 October and 15 December for days
343
344   with high and low UFP concentration (a and b) and periods A, B, and C (c and d).

345 Understanding the aerosol-cloud interactions in the region will depend on the intersection of cloud
346 formation and growth with the growth rates of the aerosol size distribution and diurnal variability in CCN
347 concentrations such as those shown in Figs. 2 and 3. Over the crest of the SDC, shallow convection
348 typically forms by the late morning. Feng et al. (2022) show that deep convective cells preferentially form
349 east of the crest between 15 and 19 UTC (12 and 16 LT), growing and intensifying until about 21 UTC
350 (18 LT). This coincides with the increase in CCN concentrations at 0.2 and 0.4% supersaturations which
351 is most pronounced on high UFP days, although peak CCN concentrations occur after most of these deep
352 convective events.

353 3.2 Sources of aerosols and trace gases observed at the ground

354 To explore the possible sources of aerosols over the AMF, we next compare aerosol composition with
355 trace gases measured at the AMF site. Not surprisingly, O_3 concentrations are relatively low (always < 45
356 ppb) at this remote site as shown in Fig. 5a. OM and O_3 are very weakly correlated (r = 0.15) even though
357 both depend on photochemical production. In contrast, the temporal variability in CO and rBC
358 concentrations over the sampling period are moderately correlated (r = 0.59) as shown by the time series

359   (Fig 5b) and scatter plot of 30-min averages (Fig. 5c). Temporal variability of CO and rBC is similar
360   because they are usually co-emitted from the same anthropogenic and/or biomass burning sources,
361   although the ratio of CO to rBC mass emitted varies from source to source. Correlations between CO and
362   rBC often approach one near the emission source; therefore, the lower correlations suggest mixing of
363   many emission sources during long-range transport and/or cloud processing of rBC containing particles
364   that leads to wet removal of rBC. OM is also moderately correlated with rBC (r = 0.56, Fig. 5d) for the
365   same reason as CO and rBC; however, biogenic sources that do not emit BC can also contribute to a
366   significant fraction of OM. Since the near-surface winds are usually from the north to northeast (Figs. S1a
367   and S1b), it is possible that a large fraction of OM, rBC, and CO originate from Córdoba and/or fires in
368   the Amazon and La Plata basins (Fig. S5a) that are transported by the low-level jet to AMF site. The
369   scatter plots in Figs. 5c and 5d are color coded by northerly (330 to 30 degrees), northeasterly (30 to 60
370   degrees), and southerly (150 to 210 degrees) wind directions show that the highest BC concentrations
371   occur during northerly winds.

372
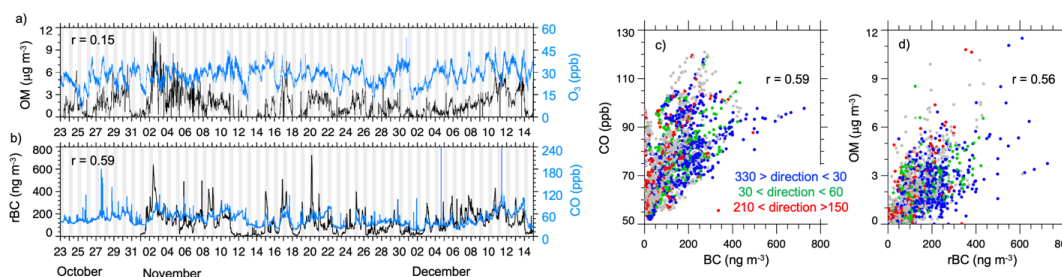
373   Figure 5.   a) Time series of a) OM and O$_3$ and b) CO and rBC between 23 October and 15 December
374   along with scatter plot of c) CO vs rBC and d) OM vs rBC.

375
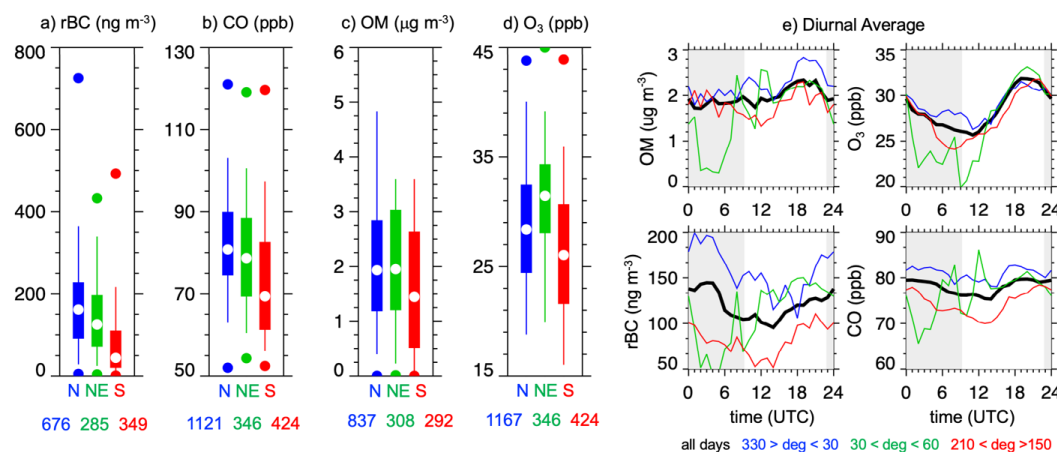
376   Figure 6.   Percentiles of a) rBC, b) CO, c) OM, and d) O$_3$ as a function of wind direction along with e)
377   the diurnal variability of these quantities as a function of wind direction.

378   The effects of wind direction are further illustrated in Fig. 6. The interquartile range of rBC and CO is
379   highest for northerly winds (Figs. 6a and 6b), followed closely by northeasterly winds. Southerly winds
380   have the lowest concentrations and a substantially lower interquartile range. For OM, the interquartile
381   ranges for northerly and northeasterly winds are similar while southerly winds have somewhat lower
382   concentrations (Fig. 6c). In contrast, O$_3$ has the highest interquartile range for northeasterly winds,

383 possibly due to transport of O₃ produced by urban emissions from Córdoba (Fig. 6d). Despite the low
384 correlation between OM and O₃, they have a similar average diurnal variability (Fig. 6e). This suggests
385 the low correlation is due primarily to multi-day variability. Maximum OM and O₃ concentrations during
386 the afternoon are ~25% and ~23% higher than at sunrise on average, respectively. OM diurnal variability
387 is also similar to the diurnal variability of CCN at 0.2% supersaturation (Fig. 3e). The average diurnal
388 variations for rBC and CO are similar with the highest values at night and lowest values a few hours after
389 sunrise. While the diurnal variability for northerly and southerly winds is similar, the concentrations are
390 significantly higher for northerly winds. OM, O₃, rBC and CO concentrations are all lowest at night for
391 northeasterly winds.

392 The CAM-Chem model is now used to illustrate transport pathways of biomass burning aerosols
393 suggested by the relationships in Figs. 5 and 6. The largest CO emissions from smoke during the
394 campaign period occur over the western Amazon basin as well as southern Brazil (Fig. S5a). Smaller fires
395 occur across most regions outside of Patagonia and the Atacama Desert. In addition to primary
396 carbonaceous particles, fires emit gas-phase aerosol precursors, including SO₂ (Fig. S5b), with emissions
397 rates that are a factor of ~2 lower than CO. These SO₂ emissions ultimately become sulfate and affect
398 CCN concentrations since sulfate is more hygroscopic than OM and rBC.

399 CAM-Chem predictions of CO and wind direction are evaluated with G-1 measurements as shown in
400 Figs. S6 and S7, respectively. The vertical and temporal variations in the vicinity of the AMF site are in
401 reasonable agreement with G-1 data, even though the coarse spatial grid does not resolve local measured
402 variations. High CO concentrations are simulated during periods of northerly and northwesterly winds,
403 suggesting that smoke from fires north of the AMF were transported over the site. Conversely, CO
404 concentrations are lower when the winds were from the south. Fires and anthropogenic emissions of CO
405 are both lower over the less populated areas of southern Argentina (Fig. S5a).

406 Since CAM-Chem is in reasonable agreement with the G-1 CO measurements, Fig. 7 shows horizontal
407 cross sections of CO at ~2.5 km MSL to illustrate transport during on episode between November 11 and
408 13. Figure 7a shows the transport of CO from the western Amazon to the AMF site by a low-level jet. A
409 trough pushes the low-level jet and plume of CO towards the east on November 12 (Fig. 7b), somewhat
410 reducing the CO concentrations. While the winds have become southerly near the AMF site, CAM-Chem
411 suggests local recirculation on the western side of the CO plume keeps the concentrations relatively high.
412 As the trough continues to propagate to the east on November 13 (Fig. 7c), lower CO from the Pacific
413 Ocean is transported over the AMF. Vertical profiles of CO from the G-1 on November 12 in Fig. 7d
414 show that the highest concentrations occur east of the SDC. This is similar to the horizontal gradient in
415 CO at 2.5 km MSL produced by CAM-Chem that shows the CO plume east of the AMF site (Fig. 7b).

416 Single particle measurements from miniSPLAT from the November 12 G-1 flight shown in Fig. 8 reveal
417 that ~12% of the particles originate from fires. The rest of the particles are composed of organics mixed
418 with varying amounts of sulfate. A large portion of the organic material not identified as biomass burning
419 aerosols is oxygenated organics, likely from biogenic sources in the Amazon that are transported by the
420 same winds to the AMF site. As noted earlier, PM1 measured by the ground ACSM was relatively low
421 between November 11 and 12 because of wet scavenging by rain and changing synoptic conditions. PM1
422 concentrations from the ACSM increased from 0.3 to 2.5 μg m⁻³ during the three-hour G-1 flight. Average
423 PM1 concentrations were 1.2 μg m⁻³, comprised of 54% OM, 19% SO₄, 11% NO₃, and 16% NH₄. While
424 bulk sulfate mass was 19% on average, the miniSPLAT data sheds light on the aerosol mixing state that
425 suggests it was mixed with ~80% of the particles. The three particle classes that have the largest fraction
426 of particles are made up of organics and sulfate at various ratios. This variability in aerosol mixing state
427 could impact CCN concentrations and aerosol optical properties (e.g., Ching et al. 2017; Saliba et al,
428 2023).

429 The circulations depicted in Fig. 7 are repeated on many days during CACTI, indicating that the AMF site
430 is periodically influenced by biomass burning. Thus, the sources of aerosols change from day to day.

431
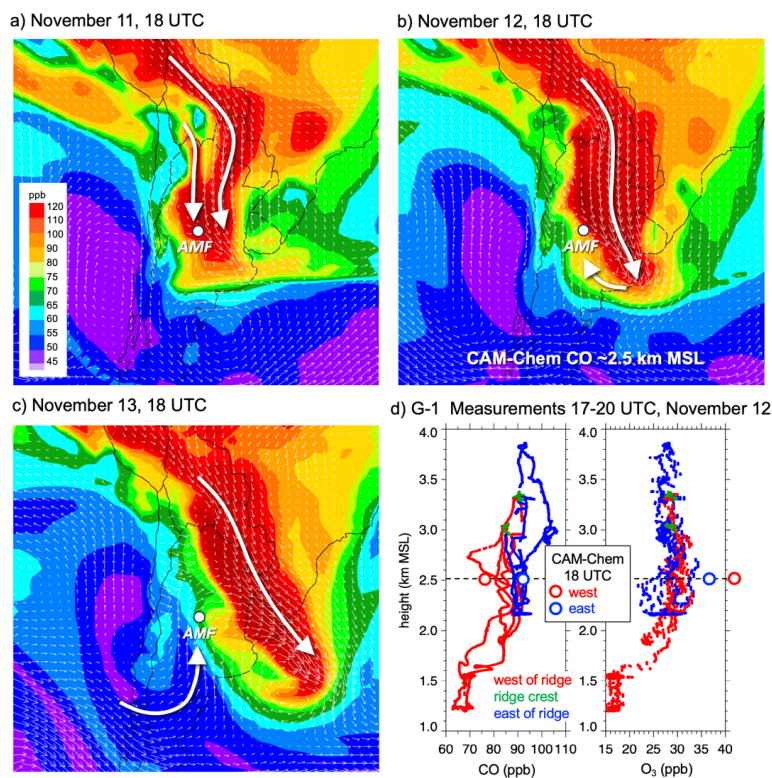
Figure 7.   CAM-Chem simulations of CO at ~2.5 km MSL at 18 UTC on a) November 11, b)
November 12, and c) November 13 along with d) vertical profiles of CO measured by the G-1
aircraft between 17 and 20 UTC on November 12.

435
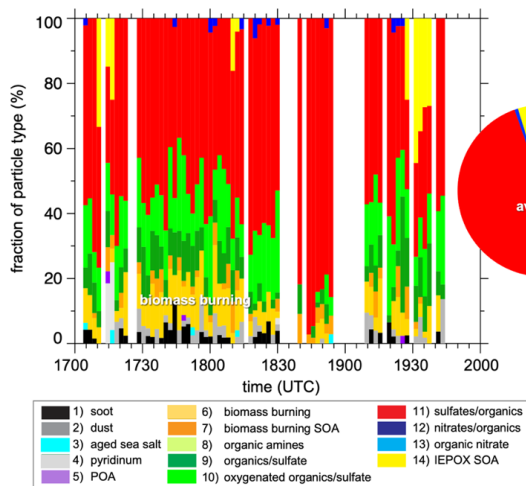
Figure 8.   Particle classes derived from the aircraft miniSPLAT mixing state measurements on
November 12.

438   3.3 Aircraft Measurements

439   The evolving size distribution of ground measured particles suggest that NPF events are followed by
440   multi-day growth to larger sizes. However, it is not clear whether these NPF events occur near the surface
441   or aloft (either in the upper boundary layer or lower free troposphere) with mixing to the surface as has
442   been observed at other locations (Chen et al. 2018; O'Donnell et al. 2023; Wang et al. 2023). Therefore, it
443   is important to examine the vertical variations in aerosol properties that are available from the G-1
444   aircraft.

445   The overall particle number concentrations observed by the two CPC instruments on flight days between
446   November 4 and December 8 are shown in Fig. 9. Median CPC concentrations are highest within 1 km of
447   the ground and then gradually become smaller with height, up to a factor of ~2.2 smaller by 3 km MSL
448   (Fig. 9a). Median concentrations increase somewhat at 3.3 km MSL and then continue to gradually
449   decrease with height so that values at 6 km MSL are almost an order of magnitude smaller than at the
450   ground. Similar trends are produced for the interquartile and 5th to 95th percentile ranges; however,
451   maximum concentrations that are between 10,000 and 100,000 cm^{-3} occur up to ~4 km MSL before
452   decreasing with height. This suggests that high concentrations of UFP could occasionally be entrained
453   into the growing daytime boundary layer and mixed to the surface. Note that number concentration
454   percentiles at 3.3 km MSL are slightly different than those at adjacent altitudes because the number of
455   samples at that altitude are much larger than any other altitude (Fig. 9b). While there are large temporal
456   variations in UFP concentrations within the G-1 flight periods as will be shown later, under-sampling is
457   not likely to affect the overall vertical variations. In addition, the number of samples above 4.5 km MSL
458   are much lower than at other altitude, so caution is warranted in interpreting the vertical variations at
459   those altitudes. Particle concentrations smaller than 10 nm, obtained by computing the differences
460   between the two CPC instruments, are similar up to 5.5 km MSL (Fig. 9c).
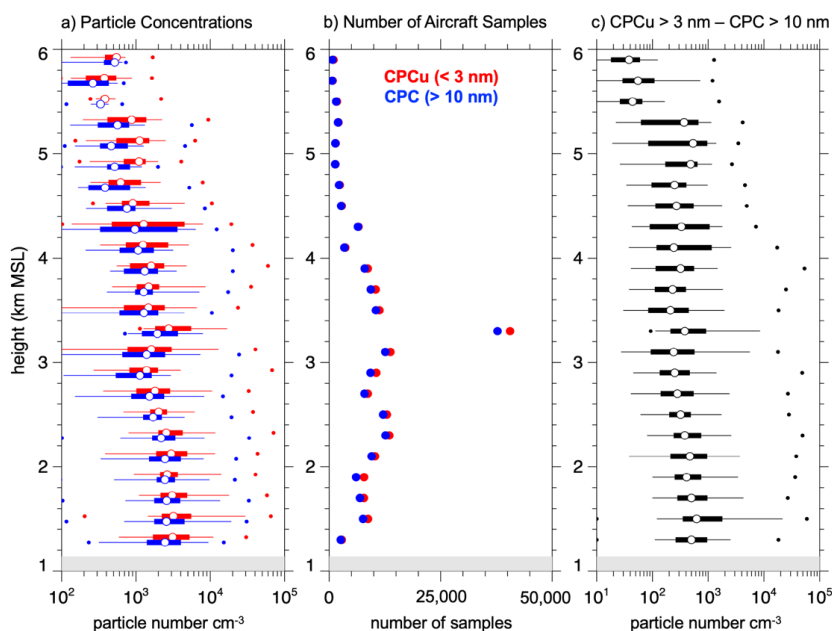
461

462   Figure 9.   a) Particle number concentration percentiles as a function of height from all the G-1
463   measurements during CACTI along with b) the number of samples at each altitude bin. c) is
464   the same as a), except for particle diameters between 3 and 10 nm.

465 Next, we examine the vertical profiles of particle concentrations in relation to the low and high UFP days
466 as determined by the surface CPC measurements. The median particle number concentrations for the
467 seven G-1 flights associated with high UFP days were higher than the median among all the G-1 flights
468 up to ~ 3 km MSL (Fig. S8). Conversely, the four G-1 flights on the low UFP days were lower than the
469 median among all the G-1 flights up to ~3 km MSL. When the G-1 flights are divided into periods A, B,
470 and C determined by the surface CPC measurements, period B has the highest median concentration near
471 the surface, followed by periods C, A, and the rainy days. The results in Fig. S8 suggest that the boundary
472 layer particle number concentrations are consistent with the broad variations seen at the ground. However,
473 it is not surprising that the trends in the surface number concentrations are not representative of the
474 temporal variability in the upper boundary layer and free troposphere.

475 A summary of the vertical profiles of CCN concentration for all the aircraft flights is shown in Fig. 10a.
476 The median CCN at 0.2% supersaturation between the surface and 3.5 km MSL varies between 255 and
477 335 cm^{-3}. At 0.5% supersaturation, CCN concentrations are about twice as high as those at 0.2% and vary
478 between 546 and 724 cm^{-3}. Above 3.5 km MSL, concentrations drop to below 100 cm^{-3} at 4 and 5.5 km
479 MSL for 0.2 and 0.5% supersaturations, respectively. The median cloud base height of 2.6 km MSL and
480 the interquartile range from KAZR-ARSCL computed during the G-1 flight periods (Fig. 10b) illustrates
481 the relevant altitudes in which CCN can be entrained into clouds. The median CCN concentrations at the
482 median cloud base height are similar to those at the surface suggesting a well-mixed boundary layer.
483 However, additional analyses are needed to determine whether surface CCN measurements are
484 representative of the conditions at cloud base at the same time as when the G-1 flew directly over the
485 AMF site.
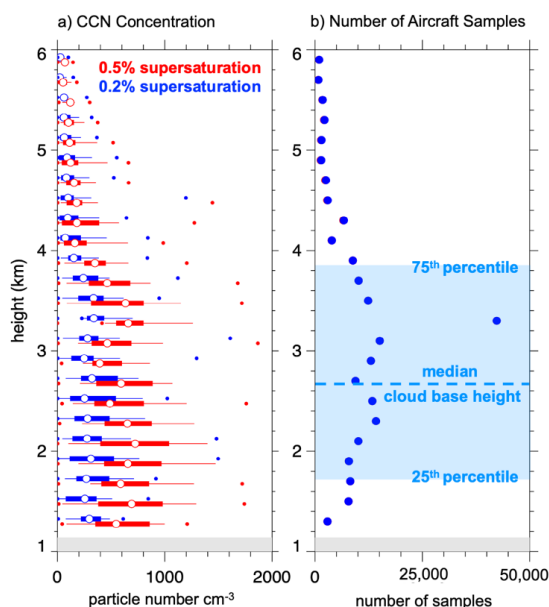
486
487 Figure 10.   a) CCN concentration percentiles as a function of height from all the G-1 measurements
488   during CACTI along with b) the number of samples at each altitude bin. Light blue shading in
489   b) denotes the 25th to 75th percentile of cloud base height observed over the AMF site.

490 Median CCN concentrations for low UFP days below 4.5 km MSL are 20 – 25% lower than the median
491 for all the flights at 0.2% supersaturation (Fig. S9a) and up to 70% lower at 0.5% supersaturation (Fig.
492 S9b). Differences in the median CCN concentrations are also produced among periods A, B, and C;
493 however, the vertical variations are noisy and suggest that additional flights are needed to account for the

494   strong spatiotemporal variations in CCN aloft. While there are only two aircraft flights on rainy days, they
495   indicate CCN concentrations are lower than all other flights within 0.3 and 1 km of the surface for 0.2%
496   and 0.5% supersaturations, respectively. Above that altitude, median CCN concentrations are similar to
497   the median of all the aircraft flights.

498   3.4 December 3 Case Study

499   The percentiles in Figs. 9 and 10 reflect both large spatial and temporal variations in CPC and CCN
500   concentrations around the AMF site. Measurements during the afternoon on December 3 are shown in
501   Fig. 11 to demonstrate the spatiotemporal variability of aerosol number, size distribution, CCN, and trace
502   gases for a particular flight. The flight path color coded by CPC concentrations indicates that particle
503   number varied by over an order of magnitude both horizontally and vertically during the 4-h flight period
504   (Fig. 11a). By comparing the flight altitude (Fig. 11b), the time series of particle number concentration
505   (Fig. 11c), and the aerosol size distribution (Fig. 11d), one can see that the highest UFP number
506   concentrations with diameters < 30 nm occurred along ~3.3 km MSL flight legs (1, 2, 5-7, 11-13, 17-19).
507   While clear skies were observed directly over the AMF site on this day, a line of orographic cumulus
508   formed over the crest of the SDC. While there was widespread cumulus over the ridge, the time spent
509   flying through clouds was less than 2.7% total time at 3.3 km MSL. There were few ultrafine particles
510   (diameters < 30 nm) for flight legs at lower (legs 3, 4, 8, 9, 20, 21) and higher (legs 14-16) altitudes. For
511   the lower and higher altitude legs, the highest particle concentrations occurred at diameters of ~80-100
512   nm and ~30-60 nm, respectively. The spatiotemporal variability in CCN concentrations (Fig. 11e) is
513   similar to the accumulation mode aerosols with the highest CCN concentrations occurring for the lowest
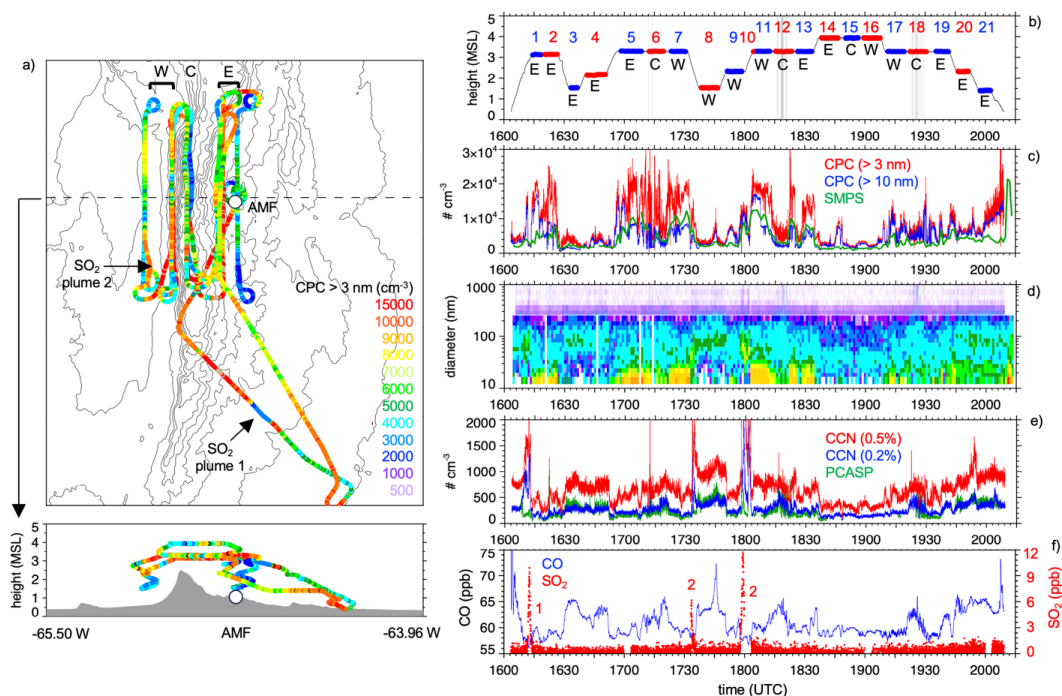
514

515   Figure 11.   a) Spatial variations in particle number concentration (> 3 nm) for the December 3 aircraft
516   flight along with temporal variations in b) altitude, c) particle number concentrations from
517   CPC and SMPS instruments, d) aerosol number distribution from BEASD, e) CCN and
518   particle number concentrations from PCASP, and f) CO and SO_2 concentrations. E, C, and W
519   in b) denote legs east of the crest, over the crest, and west of the crest as shown in a).

520   flight legs where the highest concentrations of larger particles occur. Outside of the Rio Cuarto airport,
521   the highest CO concentrations occur along the lowest flight legs (Fig. 11f) and spatiotemporal variations
522   in CO are similar to spatiotemporal variations in accumulation mode aerosols.

523   On this day, the G-1 encountered two SO_2 plumes with concentrations as high as 12 ppb denoted as
524   plume #1 and #2 in Figs. 11a and 11f. The G-1 passed through plume #2 twice at different altitudes. The
525   narrow plume width and high concentrations suggest that a local source is responsible for these two
526   plumes. Local maxima in particle number and CCN concentrations occurred at the same location as the
527   SO_2 plume, suggesting that SO_4 was also present. SO_4 is more hydrophilic than other aerosol species,
528   which may be why CCN concentrations are higher within the plume. Other than one other small plume of
529   SO_2 (~3 ppb) on December 3, no other SO_2 plumes of this magnitude were observed by the G-1 during
530   the campaign. The detection limit of the instrument is too high to describe variability of SO_2 at the ppt
531   level.

532   The advantage of the multiple constant altitude flight legs is that they can be compared to determine how
533   aerosol properties aloft evolve in time. Figure 12 depicts the variations in total particle number and CCN
534   concentrations for three periods: 1620-1730 UTC, 1806-1833 UTC, and 1911-1914 UTC, each with flight
535   legs west, over, and east of the crest of the SDC. During the first period between 1620 and 1730 UTC,
536   particle concentrations exceed 15000 cm^{-3} along most of the four flight legs (Fig. 12a). CCN
537   concentrations vary by a factor of three (300 to 900 cm^{-3}) over the region during the same period (Fig.
538   12b). The observed winds at this altitude are southerly and usually between 8 to 10 m s^{-1}.
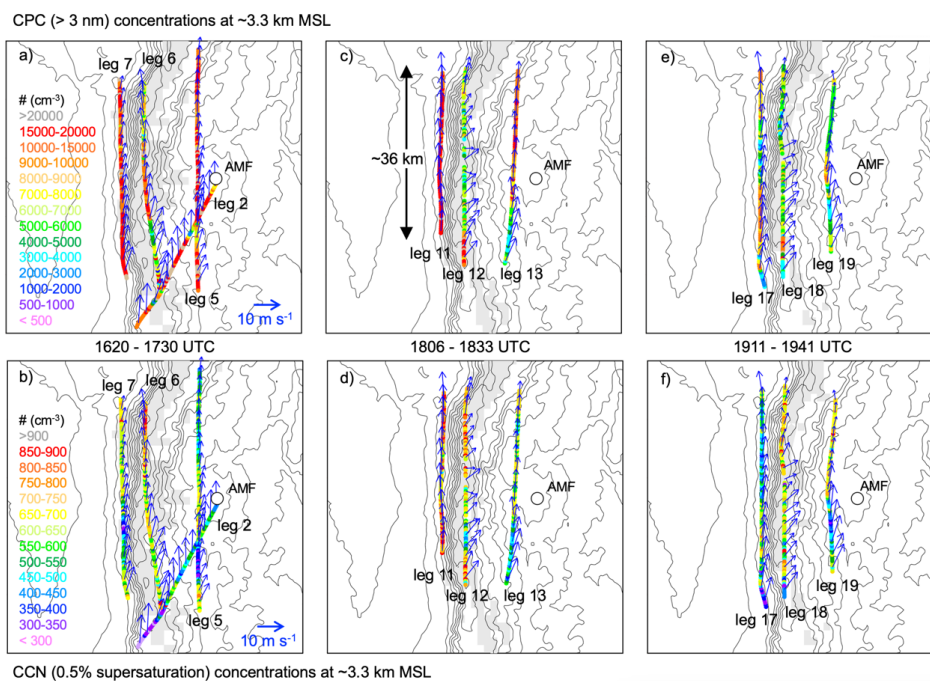
539

540   Figure 12.   Spatial variations in a) particle number concentrations > 3 nm (a, c, and e) and CCN
541   concentrations (b, d, and f) for all the ~3.3 km MSL constant altitude transects on December
542   3. Blue arrows depict wind speed and direction at 30 s intervals. Gray shading denotes cloud
543   optical depth > 2 obtained from GOES satellite (~Δx = 2 km).

544

545 The second period between 1806 and 1833 UTC took place 36 to 133 minutes after the first period;
546 therefore, aerosols sampled along legs 2, 5, 6, and 7 would be transported ~17-80 km to the north by the
547 time the aircraft conducted legs 11 to 13. Since the flight legs are ~40 km long, aerosols measured during
548 the second period are not likely to be the same as those sampled during the first period. During the second
549 period, most of the particle concentrations remain above 15000 cm^{-3} for the flight legs west and east of
550 the SDC crest (Fig. 12c). However, lower concentrations between 2000 to 5000 cm^{-3} are being
551 transported by southwesterly winds towards the AMF site along the southern third of leg 13. At this time,
552 CCN concentrations are the highest for legs 11 and 12 and lower along leg 13 closer to the AMF site (Fig.
553 12d). Interestingly, winds over the crest along legs 6 and 12 switched from southerly to southwesterly and
554 particle number concentrations became a factor of two lower between during periods one and two. As will
555 be shown in more detail later, this is likely due to both the growing boundary layer and subsidence that
556 transports lower particle number concentrations to this altitude. While winds in the lower boundary layer
557 along legs 3 and 8 and from the AMF radiosonde at 18 UTC (not shown) are from the north to northeast,
558 southwesterly winds observed near the top of the boundary layer top along leg 12 and from the 18 UTC
559 AMF radiosonde at 3.3 km reflect the wind direction shear between the boundary layer and free
560 troposphere.

561 The same wind pattern for period two persists through period three between 1911-1941 UTC. Strong
562 gradients in total aerosol number and CCN concentrations are observed for all three flight legs during this
563 period (Figs. 12e and 12f). CCN concentrations are the highest along leg 18 over the crest during period
564 three. It is possible that recycling of aerosols through clouds change the size and hygroscopicity of
565 aerosol populations and thus CCN in this region, but that requires further analysis.

566 While Fig. 12 illustrates the strong spatial and temporal variations in aerosol properties at 3.3 km MSL on
567 December 3, Fig. 13 shows the vertical variations in number and CCN concentrations that are divided into
568 flight paths west, over, and east of the crest of the SDC. West of the crest, the highest number
569 concentrations occur in two layers, one between 2.3 and 2.7 km MSL and the other between 2.9 and 3.3
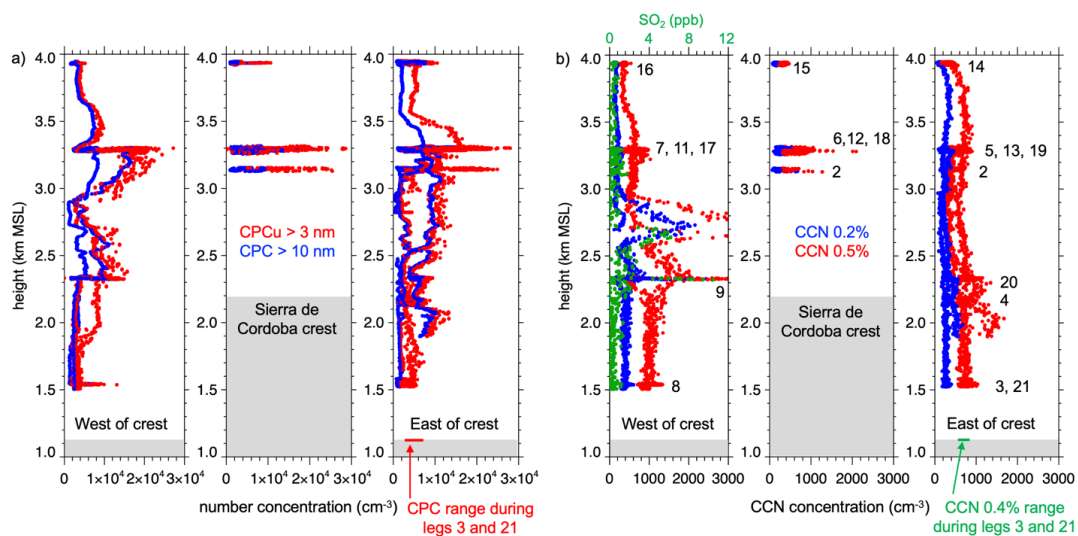
570

571 Figure 13.   Vertical variations in a) particle number concentrations and b) CCN concentrations on
572   December 3 divided into transects that are west, over, and east of the Sierras de Córdoba
573   crest. Green dots in b) denote SO2 concentrations west of the crest on December 3.

574   km MSL (Fig. 13a). Note that the smallest particles (CPC > 3 nm) concentrations vary for a given altitude
575   due to both spatial and temporal variability along the flight legs. The differences for the larger particles >
576   10 nm are much smaller at these altitudes; however, there are larger differences below 2.3 km MSL.
577   Thus, the spatial variability for UFP and larger particles is not necessarily the same. East of the crest, a
578   layer of high number concentrations occurred between 3.1 and 3.5 km MSL; however, there is not a
579   distinct second layer as seen west of the crest and the two CPC instruments have similar spatiotemporal
580   variability below 3.1 km MSL. While the spatial variability in aerosol number is similar west, over, and
581   east of the crest at 3.3 km MSL, the variability at 3.9 km MSL west of the crest is lower than over and
582   east of the crest. In general, Fig. 13 illustrates that aerosol number concentrations and variability can be
583   different west and east of the SDC crest.

584   As shown in Fig. 13b, there are also differences in CCN concentrations between the west and east sides of
585   the mountain range. There are two layers of high CCN concentrations that were sampled by the aircraft
586   west of the crest, one between 2.6 and 2.9 km MSL and the other between 2.3 and 2.5 km MSL. The
587   highest SO_2 concentrations also occur within these layers, suggesting that SO_4 produced by the SO_2
588   plume #2 (Figs. 11a and 11f) lead to higher number concentrations and more hydrophilic aerosols. SO_2
589   concentrations were low at all altitudes east of the crest. Note that the layer between 2.6 and 2.9 km MSL
590   occurs between the constant altitude transects; therefore, the spatial extent of this layer cannot be
591   determined, and other layers could be missed between the constant altitude transects. In addition, CCN
592   concentration profiles at both 0.2 and 0.5% supersaturations are somewhat lower east of the crest below
593   2.5 km MSL and somewhat higher east of the crest above 3.5 km MSL. Thus, CCN also exhibits
594   differences west and east of the crest.

595   To examine whether the aerosol size distribution is different across the SDC, the average number and
596   volume distributions as functions of altitude and location relative to the crest are shown in Fig. 14. For the
597   highest aircraft constant altitude flight legs at 3.9 km MSL, the number and volume distributions west,
598   over, and east of the crest are very similar. At 3.3 km MSL, particle number concentrations and volumes
599   for diameters less than 40 nm are the lowest over the crest and highest west of the crest. But for particles
600   greater than 80 nm in diameter, particle number concentrations are highest over the crest and the size
601   distributions for the flight legs west and east of the crest are similar. For flight legs below 2.65 km MSL,
602   there are significant differences in the number and volume distributions west and east of the crest and
603   those differences vary with height. At the lowest flight legs at 1.5 km MSL (~0.4 km above ground east of
604   the crest), the particle number concentrations and volumes for particles diameters greater than 80 nm is
605   very similar to those measured at the ground AMF site. The differences for particles smaller than 80 nm
606   indicate large spatial variability in UFP concentrations in the region. Differences between the AMF and
607   aircraft size distributions at higher altitudes suggest that the ground measurements are not representative
608   of conditions aloft. The spatiotemporal variability in size distribution likely contributes to variability in
609   CCN concentrations, similar to the differences in critical diameters shown in Fig. 4.

610   To further understand the role of boundary layer growth over the crest, we next examine variations in
611   potential temperature and vertical velocity among the 3.3 km MSL aircraft flight legs in relation to the
612   AMF radiosonde profiles as shown in Fig. 15. Between 12 and 21 UTC, the convective boundary layer at
613   the AMF site grows from 1.9 to 2.3 km MSL (Fig. 15a,b). At 21 UTC, the inflection of potential
614   temperature at ~3.3 km MSL and the higher relative humidity and southwesterly winds just below that
615   level reflect the advection of the boundary layer air from the higher terrain towards the AMF site that
616   produces a layer of constant potential temperature between 2.3 and 3.2 km MSL. The increase in potential
617   temperature between 15 to 18 UTC just above 3.3 km MSL is likely due to subsidence as southwesterly
618   air is transported across the leeward side of the crest.

619   For the flight legs between 1658 and 1731 UTC at 3.3 km MSL, variability in vertical velocity (Fig. 15c)
620   and potential temperature (Fig. 15f) is small in the free troposphere west and east of the crest. During this
621   time period, the aircraft flew just above most of the growing clouds along the ridge (leg 6). Larger
622   variations in both quantities are measured over the crest reflecting turbulent motions generated by clouds

623 just above growing boundary layer and terrain variability. By the second period between 1806 and 1833
624 UTC, spatiotemporal variations in vertical velocity (Fig. 15d) and potential temperature (Fig. 15g)
625 increase over the crest as the boundary layer grew and increased the intensity of turbulent eddies. Some of
626 the anomalies with lower potential temperatures within clouds are due to updrafts that reduce the potential
627 temperatures near the boundary layer top. High-frequency variability in vertical velocity and potential
628 temperature remains low west and east of the crest suggesting the convective boundary layer does not
629 reach 3.3 MSL for those transects over lower terrain elevations. The variability during the third period
630 between 1910-1941 UTC (Fig. 15e and 15h) is similar to the previous period. While there are few high
631 frequency variations in potential temperature west and east of the crest, there are larger-scale variations
632 likely due to larger-scale horizontal advection. For example, the southerly winds along the southern third
633 of leg 12 (Fig. 12c) between 1806 and 1833 UTC coincide with both higher potential temperature and
634 lower particle number concentrations, suggesting a different air mass. The higher potential temperatures
635 progress northward by the third period between 1920-1941 UTC.
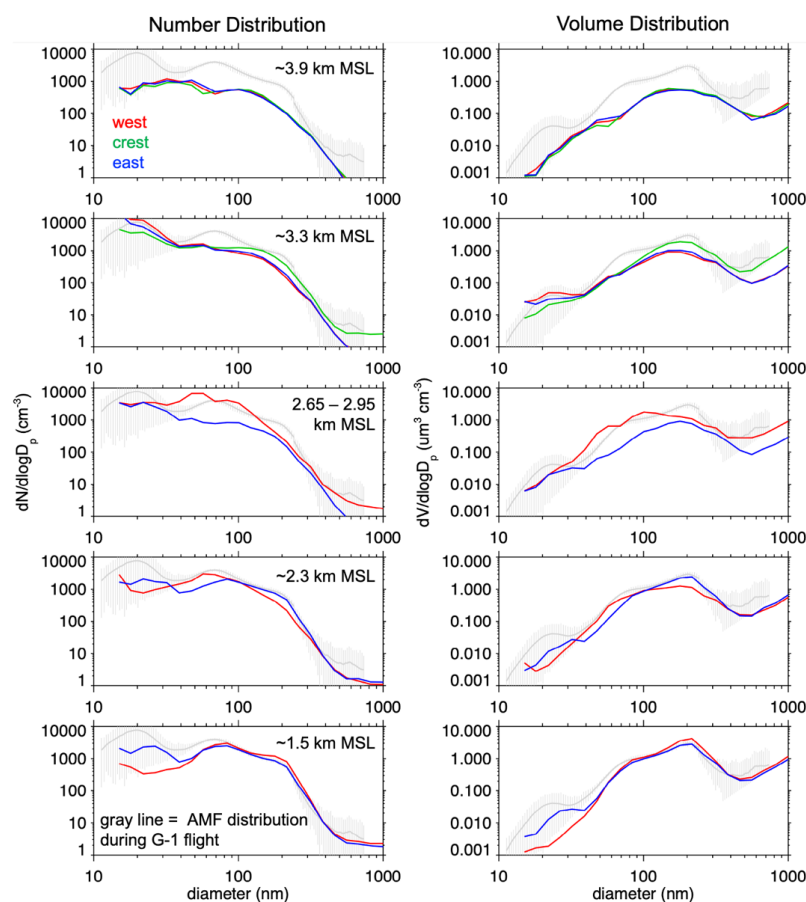
636

637 Figure 14. Number and volume aerosol distributions at five altitudes that are west, over, and east of the
638 Sierras de Córdoba crest on December 3. Gray line denotes average ground measurements
639 during the aircraft flight.
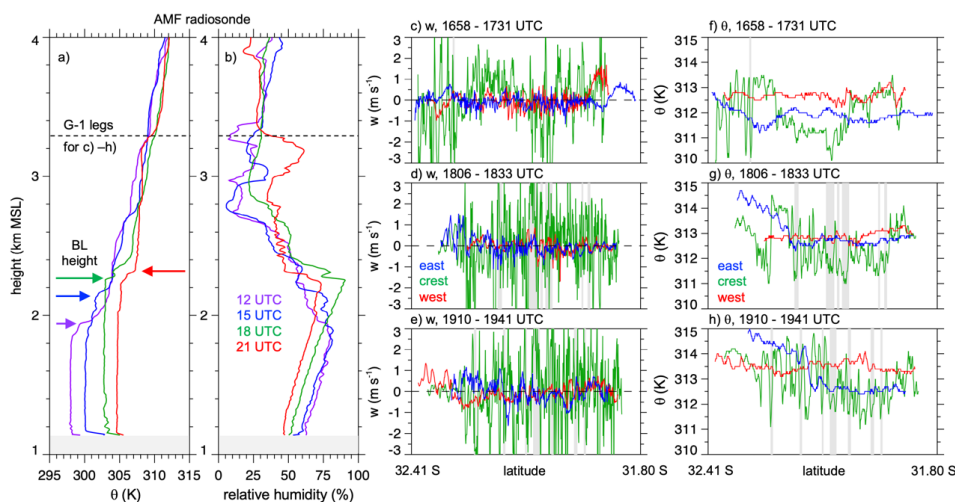
640
641
642 Figure 15.   Radiosonde profiles of a) potential temperature and b) relative humidity at the AMF site on
643   December 3 along with the spatial variations in vertical velocity c) – e) and potential
644   temperature f) – h) for G-1 flight legs at ~3.3 km MSL divided transects that are west, over,
645   and east of the Sierras de Córdoba crest. Gray shading in c) – h) denotes aircraft sampling
646   within clouds.

647 CCN concentrations shown in Fig. 16 further illustrate spatial variabilities within and among the legs
648 west, over, and east of the mountain range crest. During the first period between 1658-1731 UTC, CCN
649 concentrations at 0.2% supersaturation are higher over the crest than those along the flight legs west and
650 east of the crest (Fig. 16a). There are also larger spatial fluctuations along portions over the crest that
651 might be tied to the larger vertical velocity variations (Fig. 15c). High frequency fluctuations in CCN
652 increase as the boundary layer grows over the crest and envelopes the flight leg over the crest between
653 1806-1833 UTC (Fig. 16b). CCN concentrations at 0.2% supersaturation are still the highest with the
654 largest amount of spatial variability during the third period between 1910-1941 UTC (Fig. 16c). In the
655 free troposphere, the overall CCN concentrations west of the crest remain stable while there are large-
656 scale variations east of the crest. CCN at 0.5% supersaturation still exhibits differences between the legs
657 west, over, and east of the crest; however, CCN concentrations are not consistently higher or lower across
658 the crest during the three time periods (Figs. 16d – 16f). CCN concentrations are also lower along the
659 southern third of legs 13 and 19 east of the crest, consistent with the lower particle number concentrations
660 transported northward along legs 13 and 19 during the second and third time periods.

661 The previous figures demonstrate that local meteorological processes affect the variability in observed
662 aerosol properties. Back trajectories are used next in Fig. 17 to illustrate long-range transport pathways
663 and possible sources of aerosols transported over the AMF site on December 3. The HYSPLIT model
664 (Rolph et al., 2017; Stein et al., 2015) is used to compute 4-day back trajectories originating over the
665 AMF site at 1.5, 2.3, 2.8, and 3.3 km MSL levels and at hourly intervals between 16 and 20 UTC during
666 the G-1 aircraft flight period. Back trajectories are also computed at the corners of a 1-degree wide box
667 around the AMF site at the same altitudes and times. The trajectories are driven by winds from the
668 National Center for Environmental Prediction's Global Data Assimilation System at 0.5-degree grid
669 spacing.
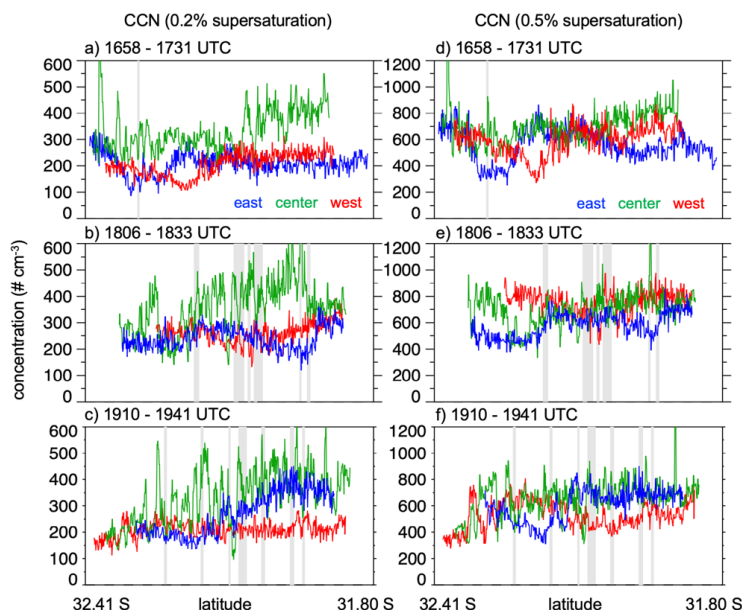
672 Figure 16.   Spatial variations in 0.2% CCN a) – c) and 0.5% CCN d) – f) for G-1 flight legs at ~3.3 km
673   MSL that are west, over, and east of the Sierras de Córdoba crest. Gray shading denotes
674   aircraft sampling within clouds.

675 Back trajectories arriving over the AMF site at 3.3 km MSL (Fig. 17a) suggest that air in the lower free
676 troposphere over the Pacific Ocean is transported by northerly to northwesterly winds toward the coast of
677 Chile. As the trajectories pass over the Andes, they become closer to the terrain (within 1.5 km MSL). It
678 is possible that anthropogenic aerosols and aerosol precursors emitted over Chile and transported by
679 upslope flows could be mixed with this air mass over the Andes. Westerly winds then transport these
680 aerosol and precursors over the Andes into Argentina and are subsequently transported by southwesterly
681 winds towards the AMF site. A similar transport pattern is produced for back trajectories originating at
682 2.8 km MSL (Fig. 17b), except that the air pass over Chile further to the south and farther from the largest
683 anthropogenic emissions. Some trajectories suggest that low emission regions over Argentina could be
684 lifted to that altitude. In contrast, back trajectories starting at 2.3 km MSL near the top of the growing
685 boundary layer are more complex (Fig. 17c). Some trajectories passing over the low anthropogenic
686 emission regions of southern Argentina are transported over the eastern slopes of the Andes where they
687 are lofted to higher altitudes and then transported by westerly winds to the AMF site. Other trajectories
688 exhibit a counterclockwise circulation so that air from southern Argentina is transported east and north of
689 the AMF site northerly winds finally transport the air masses to over the AMF site. Finally for trajectories
690 arriving near the surface at 1.5 km MSL (Fig. 17d), almost all the back trajectories exhibit the
691 counterclockwise circulation, suggesting that the lower atmosphere over the AMF is a mixture of cleaner
692 air passing over southern Argentina and higher concentrations of aerosols originating from more
693 populated regions along the Paraná River between Sante Fe and Buenos Aires.

694 Even though back trajectories do not pass over the Amazon, miniSPLAT measurements on this day
695 suggest that ~14% of the particles originate from biomass burning at all altitudes (Fig. S10). This is
696 nearly the same percentage as on November 12 when smoke was transported from more distant sources in
697 the Amazon. However, the combination of back trajectories, wind directions (Fig. S7), and low CO
698 concentrations (Figs. 11f), suggest that biomass burning from the Amazon did not contribute significantly
699 to aerosols on this day. Fire emissions inventories indicate smaller fires occurred over eastern Argentina

700 and along the coast of Chile three days prior to December 3 (not shown); therefore, the source of biomass
701 burning aerosols over the AMF site was different on November 12 and December 3. The transport time
702 also suggests that primary and secondary aerosols originating from the populated regions over eastern
703 Argentina would be aged by up to 1.5 days. In addition, the types of organic mixtures for these days were
704 very different. On December 3, the fraction of particle class 10 containing oxygenated organics and
705 sulfate mixtures was far less, particle class 11 containing the highest ratio of sulfate to organics was
706 higher on December 3, and particle class 14 containing IEPOX SOA was very small relative to November
707 12. While many of the back trajectories passed over southern Argentina, dust contributed to less than 1%
708 of the particles smaller than 1 μm in diameter on December 3.
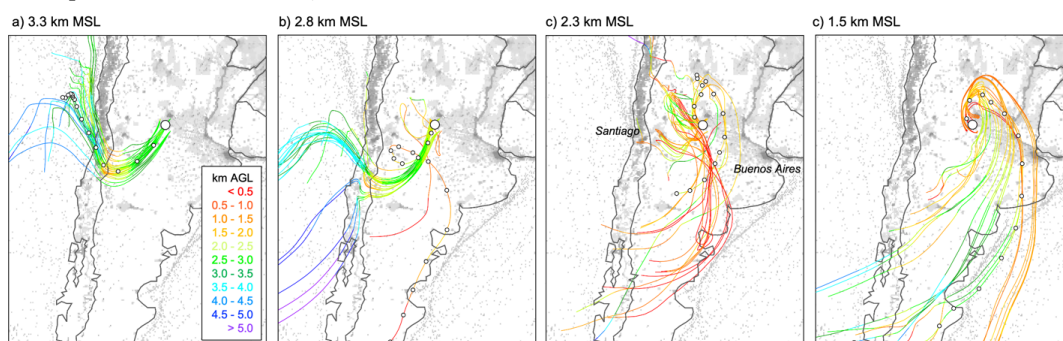
709

710 Figure 17.   Back trajectories originating at a) 3.3 km MSL, b) 2.8 km MSL, c) 2.3 km MSL, and d) 1.5
711   km MSL over the AMF site on December 3 during the G-1 flight between 16 and 20 UTC.
712   Dots denote 6-h periods along one trajectory for each height.

713 Figure 17 illustrates the impact of vertical wind shear and mountain venting processes on the transport of
714 aerosols and their precursors. The back trajectories are consistent with AMF radiosonde wind directions
715 that are northerly in the boundary layer, westerly near the boundary layer top, and southwesterly in the
716 lower free troposphere (Fig. S7). Mountain venting of aerosols and precursors into the lower free
717 troposphere results from combination of upslope flows and detrainment from the boundary layer over the
718 highest terrain (De Wekker and Kossmann, 2015) that subsequently produce layers in the lower free
719 troposphere transported far downwind. Mountain venting processes and their impact on pollutant
720 transport has been observed in many regions of the world, including the Alps (e.g. Henne et al., 2005;
721 Kossmann et al., 1999; Nyekei et al., 2000), central Mexico (Fast and Zhong, 1998), and California (e.g.
722 Fast et al., 2014; Lu and Turco, 1994; Langford et al., 2010), and Andes (e.g. Lopere et al., 2021). It is
723 important to note that the 0.5-degree grid spacing in GDAS is not likely to resolve local terrain driven
724 circulations and around the SDC and the Andes, which introduces uncertainties in these trajectories.

725 **4.   Summary and Conclusions**

726 In situ measurements of aerosol properties are needed to evaluate and improve air quality, chemical
727 transport, and climate model predictions and to better understand complex aerosol-cloud interaction
728 processes. While surface monitoring networks and aircraft field campaigns have collected aerosol
729 measurements in the northern hemisphere over the past several decades, few field campaigns with
730 extensive aerosol measurements have been conducted over subtropical and midlatitude continental areas
731 in the southern hemisphere. This study analyzes a wide range of surface and aircraft measurements
732 collected over a seven-week period during the recent CACTI field campaign in central Argentina.

733 CACTI surface observations show large multi-day variations in aerosol number, mass, composition, and
734 size distribution. On average, PM1 aerosol mass obtained from the ACSM instrument (3.7 μg m^{-3}) was
735 comprised of 53% OM, 29% SO$_4$, 8% NO$_3$, and 8% NH$_4$; however, the fraction of SO$_4$ was significantly
736 larger when PM1 mass was low (< 1 μg m^{-3}). While multiday trends in PM1 and AOD are qualitatively

737 similar and suggest most aerosol mass occurs in the boundary layer, on some days these trends differ over
738 several hours indicating that aerosol layers in the free troposphere can significantly contribute to column
739 extinction. As expected, days with the highest precipitation (October 25 - 26, November 11 – 12, and
740 November 26 – 27) have the lowest PM1 mass concentrations due to wet removal and/or changing
741 regional air masses. These rainy days divide the campaign into three periods: period A between October
742 27 and November 10 with the highest aerosol mass and lowest aerosol number concentrations, period B
743 between November 13 and 25 with the lowest aerosol mass and highest aerosol number concentrations,
744 and period C after November 28 with mass concentrations similar to period A but with aerosol number
745 concentrations between those from periods A and B. The high ultrafine particle concentrations during
746 period B, and to a lesser extent period C, suggest that new particle formation occurred over or upwind of
747 the AMF site. Average size distributions are also different among these three periods. All these
748 measurements suggest that changing mesoscale to synoptic-scale meteorology alters transport patterns as
749 well as local aerosol formation and growth processes.

750 Diurnal variation in aerosol composition, number, and CCN can be attributed to local meteorological and
751 chemical processes. While SO_4 and NH_4 showed no diurnal variability on average, peak OM, NO_3, and
752 rBC concentrations occurred during mid-afternoon, around sunrise, and at night, respectfully. The daily
753 peak in OM is likely due to photochemistry associated with SOA and the daily peak of NO_3 at sunrise
754 when the temperatures are the coldest likely inhibits partitioning of NO_3 to gas phase. Particles greater
755 than 200 nm in diameter exhibit no diurnal variations which is consistent with the weak diurnal variability
756 in PM1 mass. Conversely, smaller particles exhibit diurnal variations with a peak at ~20 UTC (17 LT),
757 and the strongest diurnal variations are for the smallest particles less than 10 nm in diameter. No diurnal
758 variability in CCN at 0.1% supersaturation was observed, consistent with little diurnal variability in
759 accumulation mode aerosols. CCN at higher supersaturations have diurnal variations with peak
760 concentrations at 22 UTC reflecting the growth of aerosols during the afternoon.

761 Potential sources of aerosols can be determined by correlating aerosol composition with trace gases and
762 wind directions. Since rBC and CO are often co-emitted, observed rBC and CO exhibits similar diurnal
763 variability and are temporally correlated (r = 0.59). The concentrations of both quantities are largest
764 during northerly winds, followed by northeasterly, with the lowest concentrations during southerly winds.
765 OM concentrations are largest for northerly and northeasterly winds with somewhat lower concentrations
766 during southerly winds. O_3 is the largest during northeasterly winds and therefore may originate from
767 anthropogenic emissions in Córdoba. The CAM-Chem global chemical transport model and single
768 particle instrument data show that biomass burning aerosols from the Amazon are frequently transported
769 by the South American low-level jet to the AMF region. Single particle measurements show that ~12% of
770 particles during one of the transport events are from biomass burning particles. Aged biogenic OM may
771 also be transported by the same winds. While SO_4 is 29% of the PM1 mass on average at the ground, it is
772 important to note that single particle measurements reveal it is mixed with organics at various ratios,
773 illustrating a more complex mixing state than from bulk measurements.

774 The aircraft measurements show that the largest total aerosol number concentrations usually occur at the
775 surface and decrease by an order of magnitude by 5 km MSL, on average. Statistics of all the flights
776 illustrate that aerosol number concentrations vary significantly (order of magnitude or more for 5th to 95th
777 percentiles) both temporally (multi-day and within 4-h flight periods) and horizontally within 50 km of
778 the AMF site at all altitudes. In contrast, average CCN concentrations remain relatively constant from the
779 surface up to 3.5 km MSL and then gradually decrease to small values by 5 km MSL. The percentiles of
780 CCN also show temporal and horizontal variability (factor of ~2 for 5th to 95th percentiles), but that
781 variability becomes small above 5 km MSL.

782 Since the aircraft data reveals large variations in aerosol properties aloft on many days, we focus on the
783 December 3 measurements as a case study. On this day, repeated constant altitude flights reveal large
784 spatial gradients in aerosol number and CCN concentrations that change from hour to hour. Two small
785 plumes of SO_2 with high aerosol number concentrations were observed; however, it is possible that the

786   aircraft could easily miss other small, transient plumes even with repeated patterns at multiple altitudes.
787   While the aerosol size distribution from the lowest flight transects east of the mountain crest and within
788   the boundary layer was similar to the ground measurements, it changed with height and was also different
789   west, over, and east of the crest of the Sierras de Córdoba range. Some flight tracks over the mountain
790   crest occurred just as the growing boundary layer intersected those altitudes, illustrating the effects of
791   aerosol entrainment across the top of the boundary layer. It is possible that cloud processing also affects
792   the size, composition, and hygroscopicity of aerosols over the mountain crest, but further analysis is
793   needed to examine this process.

794   Strong vertical wind shear at the AMF site results in transport pathways of aerosol sources that vary with
795   height. Back trajectories on December 3 indicate that aerosols within the boundary layer likely originated
796   from the more populous regions of eastern Argentina with anthropogenic and biomass burning
797   contributions. At higher altitudes mountain venting processes could produce lofting of aerosols and
798   aerosol precursors emitted from Chile or western Argentina on either side of the Andes, that is
799   subsequently transported by westerly winds over the AMF site. A similar, smaller scale process may
800   operate along the Sierras de Córdoba crest since the aircraft measurements indicate aerosols entrained into
801   the free troposphere are transported eastward over the AMF site.

802   In addition to quantifying aerosol properties in a data sparse region, the aerosol property measurements
803   presented in this study will be valuable to evaluate predictions over the mid latitudes of South America
804   and improve parameterized aerosol processes in local, regional, and global models. For aerosol-cloud
805   interaction studies, the measurements clearly show that accounting for the co-variabilities of aerosol
806   properties and convective cloud populations over the Sierras de Córdoba range will be critical. Knowing
807   aerosol properties just below and surrounding clouds is important because aerosols are entrained into the
808   base of clouds by convective updrafts. In addition to cloud base entrainment, aerosols with different
809   properties at higher altitudes are also entrained into the sides of clouds as they grow vertically. As clouds
810   evaporate, the size and composition of aerosol particles that were within cloud droplets can be different
811   than aerosol populations surrounding clouds because of cloud chemistry and coalescence of cloud
812   droplets. Thus, the properties of aerosol populations near the top of the boundary layer and arounc clouds
813   will change in time as aerosols are cycled through clouds multiple times over several hours. Given the
814   large observed variations in both aerosol and cloud properties and complexity of their interactions, it will
815   be challenging to develop a robust statistical signal of aerosol-cloud interactions from all the
816   measurements. Thus, studying impacts of aerosols on cloud properties and impacts of clouds on aerosol
817   properties on a case-by-case basis will provide critical insights.

818   **Data Availability**

819   In addition to citations given in the text, all CACTI data are available through links provided at
820   www.arm.gov/research/campaigns/amf2018cacti. Citations for individual datasets are provided
821   throughout the text.

822   **Author Contributions**

823   JF performed the data analyses and wrote the manuscript. AC was the PI of the CACTI campaign,
824   assisted in the design and interpretation of the data analyses, and contributed to the manuscript. FM, MP,
825   JT, AZ, AS, and MZ were instrument mentors during CACTI and provided comments on the manuscript
826   when they are first mentioned.

827   **Completing Interests**

828   The contact author has declared that none of the authors has any competing interests.

829   **Acknowledgments**

830   This research was supported by the U.S. Department of Energy (DOE) Office of Science, Office of
831   Biological and Environmental Research (BER) through the Atmospheric System Research (ASR)

832   program. Ground and aircraft measurements used in this study were provided by the Atmospheric
833   Radiation Measurement (ARM) Climate Research Facility, a DOE user facility sponsored by BER. The
834   Pacific Northwest National Laboratory (PNNL) is operated for DOE by Battelle Memorial Institute under
835   contract DE-AC06-76RL01830. The authors gratefully acknowledge the NOAA Air Resources
836   Laboratory (ARL) for the provision of the HYSPLIT transport and dispersion model and/or READY
837   website (https://www.ready.noaa.gov) used in this publication. CAM-Chem simulations were supported
838   by the NSF National Center for Atmospheric Research, which is a major facility sponsored by the U.S.
839   National Science Foundation under Cooperative Agreement No. 1852977.

840

References

Albrecht, B.A.: Aerosols, cloud microphysics, and fractional cloudiness, Science, 245, 1227–1230, https://doi.org/10.1126/science.245.4923.1227, 1989.

Barrett, P., Abel, S., Coe, H., Crawford, I., Dobracki, A., Haywood, J., Howell, S., Jones, A., Langridge, J., McFarquhar, G., Nott, G., Price, H., Redemann, J., Shinozuka, Y., Szpek, K., Taylor, J., Wood, R., Wu, H., Zuidema, P., Bauguitte, S., Bennett, R., Bower, K., Chen, H., Cochrane, S., Cotterell, M., Davies, N., Delene, D., Flynn, C., Freedman, A., Freitag, S., Gupta, S., Noone, D., Onasch, T., Podolske, J., Poellot, M., Schmidt, S., Springston, S., Sedlacek III, A., Trembath, J., Vance, A., Zawadowicz, M., and Zhang, J.: Intercomparison of airborne and surface-based measurements during the CLARIFY, ORACLES and LASIC field experiments." Atmos. Meas. Tech., 15, 6329-6371, https://doi.org10.5194/amt-15-6329-2022, 2022.

Borque, P.A., Varble, A.C., and Hardin, J., Peak rain rate sensitivity to observed cloud condensation nuclei and turbulence in continental warm shallow clouds during CACTI, J. Geophys. Res., 127, E2022JD036864, https://doi.org/10.1029/2022JD036864, 2022.

Brock, C.A., Williamson, C., Kupc, A., Froyd, K.D., Erdesz, F., Wagner, N., Richardson, M., Schwarz, J.P. Gao, R.-S., Katich, J.M., Campuzano-Jost, P., Nault, B.A., Schroder, J.C., Jimenez, J.L., Weinzier, B., Dollner, M., Bui, T., and Murphy, D.M.: Aerosol size distributions during the Atmospheric Tomography Mission (ATom): Methods, uncertainties, and data products, Atmos. Meas. Tech., 12, 3081-3099, https://doi.org//10.5194/amt-12-3081-2019. 2019.

Burk, K., and Ermold, B.: Carbon Monoxide - Airborne (AAFCO), Atmospheric Radiation Measurement (ARM) User Facility, https://doi.org/10.5439/1488849, Last accessed 15 April 2024, 2018.

Burk, K., Ermold, B., and Trojanowski, R.: Sulfur Dioxide Monitor aboard Aircraft (AAFSO2), Atmospheric Radiation Measurement (ARM) User Facility, https://doi.org/10.5439/1488850, Last accessed 15 April 2024, 2018a.

Burk, K., Ermold, B., and Trojanowski, R.: Ozone Monitor aboard Aircraft (AAFO3), Atmospheric Radiation Measurement (ARM) User Facility, https://doi.org/10.5439/1488851, Last accessed 15 April 2024, 2018b.

Carslaw, K.S., Lee, L.A., Regayre, L.A., and Johnson, J.S., Climate models are uncertain, but we can do something about it, Eos., 99. http://doi.org/10.1029/2018EO093757, 2018.

Chen, H., Hodshire, A.L., Ortega, J., Greenberg, J., McMurry, P.H. Carlton, A.G., Pierce, J.R., Hanson, D.R., and Smith, J.N.: Vertically resolved concentration and liquid water content of atmospheric nanoparticles at the US DOE Southern Great Plains site, Atmos. Chem. Phys., 18, 311-326, https://doi.org/10.5194/acp-18-311-2018, 2018.

Ching, J., Fast, J., West, M., and Riemer, N.: Metrics to quantify the importance of mixing state for CCN activity, Atmos. Chem. Phys., 17, 7445–7458, https://doi.org/10.5194/acp-17-7445-2017, 2017.

Cromwell, E., Tomlinson, J., and Pekour, M.: Cloud and Aerosol Spectrometer aboard aircraft (AAFCAS), Atmospheric Radiation Measurement (ARM) User Facility, https://doi.org/10.5439/1438488. Last accessed 15 April 2024, 2018.

Danabasoglu, G., Lamarque, J.-F., Bachmeister, J., Bailey, D.A., DuVivier, A.K., Edwards, J., Emmons, L.K., Fasullo, J., Garcia, R., Gettelman, A., Hannay, C., Holland, M.M., Large, W.G., Lawrence, D.M., Lenaerts, J.T.M., Lindsay, K., Lipscomb, W.H., Mills, M.J., Neale, R., Oleson, K.W., Otto-Bliesner, B., Phillips, A.S., Sacks, W., Tilmes, S., van Kampenhout, L., Vertenstein, M., Bertini, A., Dennis, J., Deser, C., Fischer, C., Fox-Kember, B., Kay, J.E., Kinnison, D., Kushner, P.J., Long, M.C., Mickelson, S., Moore, J.K., Nienhouse, E., Polvani, L., Rasch, P.J., and Strand, W.G: The Community Earth System Model version 2 (CESM2), J. Adv. Model. Earth Sys., 12, https://doi.org/10.1029/2019MS001916, 2019.

886 DeCarlo, P.F., Kimmel, J.R., Trimborn, A., Northway, M.J., Jayne, J.T., Aiken, A.C., Gonin, M., Fuhrer,
887 K., Horvath, T., Docherty, K.S., Worsnop, D.R., and Jimenez, J.L.: Field-deployable, high-resolution,
888 time-of-flight aerosol mass spectrometer, Anal. Chem., 78, 8281–8289,
889 https://doi.org/10.1021/ac061249n, 2006.

890 De Wekker, S.J.F., and Kossman, M.: Convective boundary layer heights over mountainous terrain – A
891 review of concepts, Front. Earth Sci., 3, https://doi.org/10.3389/feart.2015.00077, 2015.

892 Emmons, L.K., Schwantes, R.H.,Orlando, J.J., Tyndall, G., Kinnison, D., Lamarque, J.-F., Daniel Marsh
893 D., Mills, M.J., Tilmes, S., Bardeen, C., Buchholz, R.R., Conley, A., Gettelman, A., Garcia, R., Simpson,
894 I., Blake, D.R., Meinardi, S., and Pétron, G.: The chemistry mechanism in the Community Earth System
895 Model version 2 (CESM2). J. Adv. Model. Earth Sys., 12, e2019MS001882.
896 https://doi.org/10.1029/2019MS001882, 2020.

897 Fan, J., Wang, Y., Rosenfeld, D., and Liu, Y., Review of aerosol–cloud interactions: Mechanisms,
898 significance, and challenges, J. Atmos. Sci., 73, 4221-4252, https://doi.org/10.1175/JAS-D-16-0037.1,
899 2016.

900 Fast, J.D., Allan, J. Bahreini, R., Craven, J., Emmons, L., Ferrare, R., Hayes, P.L., Hodzic, A., Holloway,
901 J., Hostetler, C., Jimenez, J.L., Jonsson, H., Liu, S., Liu, Y., Metcalf, A., Middlebrook, A., Nowak, J.,
902 Pekour, M., Perring, A., Pollack, I., Russell, L., Ryerson, T., Sedlacek, A., Seinfeld, J., Setyan, A.,
903 Shilling, J., Shrivastava, M., Springston, S., Song, C., Subramanian, R., Taylor, J.W., Vinoj, V., Warneke,
904 C., Yang, Q., Zaveri, R.A., and Zhang, Q.: Modeling regional aerosol variability over California and its
905 sensitivity to emissions and long-range transport during the 2010 CalNex and CARES campaigns, Atmos.
906 Chem. Phys., 14, 10013-10060. https://doi.org/10.5194/acp-14-10013-2014, 2014.

907 Fast, J.D., Bell, D.M., Kulkarni, G., Liu, J., Mei, F., Saliba, G., Shilling, J.E., Suski, K., Tomlinson, J.,
908 Wang, J., Zaveri, R., and Zelenyuk, A.: Using aircraft measurements to characterize subgrid-scale
909 variability of aerosol properties near the ARM southern Great Plains site. Atmos. Chem. Phys., 22,
910 11271-11238, https://doi.org/10.5194/acp-22-11217-2022, 2022.

911 Fast, J.D., and Zhong, S.Y.: Meteorological factors associated with inhomogeneous ozone concentrations
912 within the Mexico City basin, J. Geophys. Res., 103, 18927–18946. https://doi.org/10.1029/98JD01725,
913 1998.

914 Feingold, G., Ghate, V.P., Russell, L.M., Blossey, P., Cantrell, W., Christensen, M.W., Diamond, M.S.,
915 Gettelman, A., Glassmeier, F., Gryspeerdt, E., Haywood, J., Hoffmann, F., Kaul, C.M., Lebsock, M.,
916 McComiskey, A.C., McCoy, D.T., Ming, Y., Mülmenstädt, J., Possner, A., Prabhakaran, P., Quinn, P.K.,
917 Schmidt, K.S., Shaw, R.A., Singer, C.E., Sorooshian, A., Toll, V., Wan, J.S., Wood, R., Yang, F., Zhang,
918 J., and Zheng, X.: Physical science research needed to evaluate the viability and risks of marine cloud
919 brightening, Sci. Adv., 10, eadi8594, https://doi.org/10.1126/sciadv.adi8594, 2024.

920 Feng, Z., Hardin, J., Barnes, H.C., Li, J., Leung, L.R., Varble, A.C., and Zhang, Z.: PyFLEXTRKR: A
921 flexible feature tracking python software for convective cloud analysis, Geosci. Model Devel., 16, 2753-
922 2776, https://doi.org/10.5194/gmd-16-2753-2023, 2023.

923 Feng, Z., Varble, A.C., Hardin, J.C., Marquis, J.N., Hunzinger, A., Zhang, Z., and Thieman, M.: Deep
924 convection initiation, growth and environments in the complex terrain of central Argentina during
925 CACTI, Mon. Wea. Rev., 150, 1135-1155. https://doi.org/10.1175/MWR-D-21-0237.1, 2022.

926 Henne, S., Dommen, J., Neininger, B., Reimann, S., Staehelin, J., and Prévôt, A.S.H.: Influence of
927 mountain venting in the Alps on the ozone chemistry of the lower free troposphere and the European
928 pollution export, J. Geophys. Res., 110, D22307, http://doi.org/10.1029/2005JD005936, 2005.

929 Johnson, K., Jensen, M., and Giangrande, S.: Active Remote Sensing of CLouds (ARSCL) product using
930 Ka-band ARM Zenith Radars (ARSCLKAZRBND1KOLLIAS), Atmospheric Radiation Measurement
931 (ARM) User Facility, https://doi.org/10.5439/1228769, Last accessed 15 April 2024, 2018.

932   Keeler, E., Burk, K., and Kyrouac, J.: Balloon-Borne Sounding System (SONDEWNPN). Atmospheric
933   Radiation Measurement (ARM) User Facility. https://doi.org/10.5439/1595321, Last accessed 15 April
934   2024, 2018.

935   Kohler, H.: The nucleus in and the growth of hygroscopic droplets, Trans. Farad. Soc., 32, 1152–1161,
936   1936.

937   Koontz, A., Flynn, C., and Shilling, J.: Aerosol Optical Depth (AOD) derived from MFRSR
938   measurements (MFRSRAOD1MICH), Atmospheric Radiation Measurement (ARM) User Facility,
939   https://doi.org/10.5439/1356805, Last accessed 15 April 2024, 2018a.

940   Koontz, A., Flynn, C., Kuang, C., Andrews, E., Hayes, C., Singh, A., and Salwen, C.: Condensation
941   Particle Counter (AOSCPCU), Atmospheric Radiation Measurement (ARM) User Facility,
942   https://doi.org/10.5439/1228061, Last accessed 15 April 2024, 2018b.

943   Koontz, A., Kuang, C., Andrews, E., Hayes, C., Singh, A., and Salwen, C.: Condensation Particle
944   Counter (AOSCPCF), Atmospheric Radiation Measurement (ARM) User Facility,
945   https://doi.org/10.5439/1352536, Last accessed 15 April 2024, 2018c.

946   Koontz, A., Uin, J., Andrews, E., Enekwizu, O., Hayes, C., & Salwen, C.: Cloud Condensation Nuclei
947   Particle Counter (AOSCCN2COLA). Atmospheric Radiation Measurement (ARM) User Facility.
948   https://doi.org/10.5439/1323892, Last accessed 15 April 2024, 2018d.

949   Koontz, A., Uin, J., Andrews, E., Enekwizu, O., Hayes, C., and Salwen, C.: Cloud Condensation Nuclei
950   Particle Counter (AOSCCN2COLB), Atmospheric Radiation Measurement (ARM) User Facility,
951   https://doi.org/10.5439/1323893, Last accessed 15 April 2024, 2018e.

952   Koontz, A., Springston, S., and Trojanowski, R.: Carbon Monoxide Analyzer (AOSCO), Atmospheric
953   Radiation Measurement (ARM) User Facility, https://doi.org/10.5439/1250819, Last accessed 15 April
954   2024, 2018f.

955   Koontz, A., Mei, F., Stephenson, J., and Pekour, M.: Condensation particle counter aboard aircraft
956   (AAFCPCU), Atmospheric Radiation Measurement (ARM) User Facility,
957   https://doi.org/10.5439/1349237, Last accessed 15 April 2024, 2018g.

958   Koontz, A., Mei, F., Stephenson, J., and Pekour, M.: Condensation particle counter aboard aircraft
959   (AAFCPCFISO), Atmospheric Radiation Measurement (ARM) User Facility,
960   https://doi.org/10.5439/1373109, Last accessed 15 April 2024, 2018h.

961   Koontz, A., Mei, F., and Pekour, M.: Cloud Condensation Nuclei Particle Counter aboard Aircraft
962   (AAFCCN2COLA), Atmospheric Radiation Measurement (ARM) User Facility,
963   https://doi.org/10.5439/1349242, Last accessed 15 April 2024, 2018i.

964   Koontz, A., Mei, F., and Pekour, M.: Cloud Condensation Nuclei Particle Counter aboard Aircraft
965   (AAFCCN2COLB), Atmospheric Radiation Measurement (ARM) User Facility,
966   https://doi.org/10.5439/1349243, Last accessed 15 April 2024, 2018j.

967   Kossmann, M., Corsmeier, U., de Wekker, S.F.J., Fiedler, F., Vögtlin, R., Kalthoff, N., Güsten, H.,
968   Neininger, B., Observations of handover processes between the atmospheric boundary layer and the free
969   troposphere over mountainous terrain, Contr. Atmos. Phys., 72, 329–350, 1999.

970   Kuang, C., Singh, A., Howie, J., Salwen, C., and Hayes, C.: Scanning mobility particle sizer
971   (AOSSMPS), Atmospheric Radiation Measurement (ARM) User Facility,
972   https://doi.org/10.5439/1476898, Accessed Day Month Year, 2018.

973   Kulkarni, G., Levin, M., and Shilling, J.: CCN Counter derived hygroscopicity parameter kappa
974   (AOSCCNSMPSKAPPA), Atmospheric Radiation Measurement (ARM) User Facility,
975   https://doi.org/10.5439/1729907, Accessed Day Month Year, 2018

976 Kulkarni, G., Mei, F., Shilling, J., Wang, J., Reveggino, R., Flynn, C., Zelenyuk, A., and Fast, J.D.: Cloud
977 condensation nuclei closure study Using airborne measurements over the southern Great Plains, J.
978 Geophys. Res., 128, e2022JD037964, https://doi.org/10.1029/2022JD037967, 2023.

979 Kyrouac, J., Shi, Y., and Tuftedal, M.: Surface Meteorological Instrumentation (MET). Atmospheric
980 Radiation Measurement (ARM) User Facility. https://doi.org/10.5439/1786358, Last accessed 15 April
981 2024, 2018.

982 Langford, A.O., Senff, C.F., Alvarez, R.J., Banta, R.M., and Hardesty, R.M.: Long-range transport of
983 ozone from the Los Angeles Basin: A case study. Geophy. Res. Lett., 37, L06807,
984 https://doi.org/10.1029/2010GL042507, 2010.

985 Lopere, R., Muller, S., Menut, L., and Huneeus, N.: Pathways for wintertime deposition of anthropogenic
986 light-absorbing particles on the Central Andes cryosphere, Environ. Pollution, 272, 115901,
987 https://doi.org/10.1016/j.envpol.2020.115901, 2021.

988 Lu, R., and Turco, R.P.: Air pollutant transport in a coastal environment, J. Atmos. Sci., 51, 2285-2308,
989 https://doi.org/10.1175/1520-0469(1994)051<2285:APTIAC>2.0.CO;2, 1994.

990 Liu, X., Ma, P.-L., Wang, H., Tilmes, S., Singh, B., Easter, R.C., Ghan, J.S., and Rasch, P.J.: Description
991 and evaluation of a new four-mode version of the Modal Aerosol Module (MAM4) within version 5.3 of
992 the Community Atmosphere Model, Geosci. Model Dev., 9, 505-522. https://doi.org/10.5194/gmd-9-505-
993 2016, 2016.

994 Marinovici, C., and Tomlinson, J.: Passive cavity aerosol spectrometer aboard aircraft (AAFPCASP),
995 Atmospheric Radiation Measurement (ARM) User Facility, https://doi.org/10.5439/1245509, Last
996 accessed 15 April 2024, 2018.

997 Marquis, J.N., Varble, A.C., Robinson, P. Nelson, T.C., and Friedrich, K.: Low-level mesoscale and
998 cloud-scale interactions promoting deep convection initiation, Mon. Wea. Rev., 149, 2473–2495,
999 https://doi.org/10.1175/MWR-D-20-0391.1, 2021.

1000 Marquis, J.N., Feng, Z., Varble, A.C., Nelson, T.C., Houston, A., Peters, J.M., Mulholland, J.P., and
1001 Hardin, J.: Near-cloud atmospheric ingredients for deep convection initiation, Mon. Wea. Rev., 51, 1247–
1002 1267, https://doi.org/10.1175/MWR-D-22-0243.1, 2023.

1003 Martin, S., Artaxo, P., Machado, L., Manzi, A., Souza, R., Schumacher, C., Wang, J., Brito, J., Jardine,
1004 K., Medeiros, A., de Sa, T. Biscaro, S., Calheiros, A., Potela, B., Adachi, K., Aiken, A., Albrecht, R.,
1005 Alexander, L., Andreae, R., Barbosa, H., Buseck, P., Chand, D., Comstock, J., Dubey, M., Fan, J., Fast,
1006 J., Fisch, G., Fortner, E., Giagrande, S., Gilles, M., Goldstein, A., Guenther, A., Hubbe, J., Jensen, M.,
1007 Jimenez, J., Keutsch, F., Kim, S., Kuang, C. Laskin, A., McKinney, K., Mei, F., Miller, M., Nascimento,
1008 R., Pauliquevis, T., Pekour, M., Peres, J., Petaja, T., Pohlder, C., Poschl, U., Rizzo, L., Schmid, B.,
1009 Shilling, J., Dias, M.A.S., Smith, J., Tomlinson, J., Tota, J., and Wendisch, M.: The green ocean Amazon
1010 experiment (GoAmazon2014/5) observes pollution affecting gases, aerosols, clouds, and rainfall over the
1011 rain forest, Bull. Amer. Meteor. Soc., 98, 981-997. https://doi.org/10.1175/BAMS-D-15-00221.1, 2017.

1012 Mather, J.H., and Voyles, J.W.: The ARM Climate Research Facility: A review of structure and
1013 capabilities. Bull. Amer. Meteor. Soc., 94, 377–392. https://doi.org/10.1175/BAMS-D-11-00218.1, 2013.

1014 McFarquhar, G.M., Bretherton, C.S., Marchand, R., Protat, A., DeMott, P.J., Alexander, S.P., Roberts,
1015 G.C., Twohy, C.H., Toohey, D., Siems, S., Huang, Y., Wood, R., Rauber, R.M., Lasher-Trapp, S., Jensen,
1016 J., Stith, J.L., Mace, J., Um, J., Järvinen, E., Schnaiter, M., Gettelman, A., Sanchez, K.J., McCluskey,
1017 C.S., Russell, L.M., McCoy, L.L., Atlas, R.L., Bardeen, C.G., Moore, K.A., Hill, T.C.J., Humphries, R.S.,
1018 Keywood, M.D., Ristovski, Z., Cravigan, L., Schofield, R., Fairall, C., Mallet, M.S., Kreidenweis, S.M.,
1019 Rainwater, B., D'Alessandro, J., Wang, Y., Wu, W., Saliba, G., Levin, E.J.T., Ding, S., Lang, F., Truong,
1020 S.C.H., Wolff, C., Haggerty, J., Harvey, M.J., Klekociuk, A.R., and McDonald, A.: Observations of
1021 Clouds, Aerosols, Precipitation, and Surface Radiation over the Southern Ocean: An Overview of

CAPRICORN, MARCUS, MICRE, and SOCRATES, Bull. Amer. Meteor. Soc., 102, E894-E928, https://doi.org/10.1175/BAMS-D-20-0132.1, 2021.

Mei, F., Burk, K., Ermold, B., and Zhang, D.: Fast Cloud Droplet Probe aboard aircraft (AAFFCDP), Atmospheric Radiation Measurement (ARM) User Facility, https://doi.org/10.5439/1417472, Last accessed 15 April 2024, 2018.

Mei, F., and Pekour, M.: Scanning mobility particle sizer aboard aircraft (AAFSMPS), Atmospheric Radiation Measurement (ARM) User Facility, https://doi.org/10.5439/1961525, Last accessed 15 April 202, 2018.

Nelson, T.C., Marquis, J., Peters, J., and Friedrich, K.: Environmental controls on simulated deep moist convection initiation occurring during RELAMPAGO-CACTI, J. Atmos. Sci., 79, 1941-1964, https://doi.org/10.1175/JAS-D-21-0226.1, 2022.

Nesbitt, S.W., Salio, P.V., Ávila, E., Bitzer, P., Carey, L., Chandrasekar, V., Deierling, W., Dominguez, F., Dillon, M.E., Garcia, C.M., Gochis, D., Goodman, S., Hence, D.A., Kosiba, K.A., Kumjian, M.R., Lang, T., Luna, T.M., Marquis, J., Marshall, R., McMurdie, L.A., de Lima Nascimento, E., Rasmussen, K..L., Roberts, R., Rowe, A.K., Ruiz, J.J., São Sabbas, E.F.M.T., Saulo, A.C., Schumacher, R.S., Skabar, Y.G., Machado, L.A.T., Trapp, R.J., Varble, A.C.., Wilson, J., Wurman, J., Zipser, E.J., Arias, I., Bechis, H., and Grover, M.A.: A storm safari in subtropical South America: Proyecto RELAMPAGO, Bull. Amer. Meteor. Soc., 102, E1621–E1644, https://doi.org/10.1175/BAMS-D-20-0029.1, 2021.

Ng, N.L., Herndon, S.C., Trimborn, A., Canagaratna, M.R., Croteau, P.L., Onasch, T.B., Sueper, D., Worsnop, D.R., Zhang, Q. Sun, Y.L., and Jayne, J.T.: An aerosol chemical speciation monitor (ACSM) for routine monitoring of the composition and mass concentrations of ambient aerosol, Aerosol Sci. Tech., 45, 780-794, https://doi.org/10.1080/02786826.2011.560211, 2011.

Nyeki, S., Kalberer, M., Colbeck, I., De Wekker, S., Furger, M., Gäggeler, H.W., Kossmann, M., Lugauer, M., Steyn, D., Weingartner, E., Wirth, M., and Baltensperger, U.: Convective boundary layer evolution to 4 km asl over High-alpine terrain: Airborne lidar observations in the Alps, Geophys. Res. Lett., 27, 689-692, https://doi.org/10.1029/1999GL010928, 2000.

O'Donnell, S.E., Akherati, A., He, Y., Hodshire, A.L., Shilling, J.E., Kuang, C., Fast, J.D. Fast, Mei, F., Schobesberger, S., Thornton, J.A., Smith, J.N., Jathar, S.H., and Pierce, J.R.: Look up: Probing the vertical profile of new particle formation and growth in the planetary boundary layer with models and observations, J. Geophys. Res., 128, e2022JD037525, https://doi.org.10.1029/2022JD037525. 2023.

Pekour, M., and Ermold, B.: Aerosol Size Distribution Best Estimate from sensors aboard aircraft (AAFMERGEDAEROSOLSD), Atmospheric Radiation Measurement (ARM) User Facility, https://doi.org/10.5439/1905541, Last accessed 15 April 2024, 2023.

Petters, M.D., and Kriedenweis. S.M.: A single parameter representation of hygroscopic growth and cloud condensation nucleus activity, Atmos. Chem. Phys. 7, 1961-1971, https://doi.org/10.5194/acp-7-1961-2007, 2007.

Reddington, C.L., Carslaw, K.S., Stier, P., Schutgens, N., Coe, H., Liu, D., Allan, J., Browse, J., Pringle, K.J., Lee, L.A., Yoshioka, M., Johnson, J.S., Regayre, L.A., Spracklen, D.V., Mann, G.W., Clarke, A., Hermann, M., Henning, S., Wex, H., Kristensen, T.B., Leaitch, W.R., Pöschl, U., Rose, D., Andreae, M.O., Schmale, J., Kondo, Y., Oshima, N., Schwarz, J.P., Nenes, A., Anderson, B., Roberts, G.C., Snider, J.R., Leck, C., Quinn, P.K., Chi, X., Ding, A., Jimenez, J.L., and Zhang, Q.: The Global Aerosol Synthesis and Science Project (GASSP): Measurements and modeling to reduce uncertainty, Bull. Amer. Meteor. Soc., 98, 1857-1877, https://doi.org/10.1175/bams-d-15-00317.1, 2017.

Rolph, G., Stein, A., and Stunder. B.: Real-time Environmental Applications and Display sYstem: READY, Environ. Model. Software., 95, 210-228. https://doi.org/10.1016/j.envsoft.2017.06.025, 2017.

Rosenfeld, D., Andreae, M.D., Chin, A.A.M., de Leeuw, G., Donovan, D.P., Kahn, R., Kinne, S., Kivekäs, N., Kulmala, M., Lau, W., Schmidt, K.S., Suni, T., Wagner, T., Wild, M., and Quaas, J.: Global observations of aerosol-cloud-precipitation-climate interactions. Rev. Geophys., 52, 750–808. https://doi.org/10.1002/2013RG000441, 2014.

Saliba, G., Bell, D., Suski, K., Fast, J., Imre, D., Kulkarni, G., Mei, F., Muelmenstaedt, J.H., Pekour, M., Shilling, J.E., Tomlinson, J., Varble, A.C., Thornton, J.A., and Zelenyuk, A.: Aircraft measurements of single particle size and composition reveal aerosol size and mixing state dictate their activation into cloud droplets, Environ. Sci. Atmos., 3, 1352, DOI:10.1039/D3EA00052D, 2023.

Sasaki, C.R.S., Rowe, A.K., McMurdie, L.A., Varble, A.C., and Zhang, Z.: Influences of the South American low-level jet on the convective environment in central Argentina using a convection-Permitting simulation, Mon. Wea. Rev., https://doi.org/10.1175/MWR-D-23-0122.1, 2024.

Schmid, B., Tomlinson, J.M., Hubbe, J.M., Comstock, J.M., Mei, F., Chand, D., Pekour, M.S., Kluzek, C.D., Andrews, E., Biraud, S.C., and McFarquhar, G.M.: The DOE ARM Aerial Facility, Bull. Amer. Meteor. Soc., 95, 723-742. https://doi.org/10.1175/BAMS-D-13-00040.1. 2014.

Schwarz, J.P., Gao, R.S., Fahey, D.W., Thomson, D.S., Watts, L.A., Wilson, J.C., Reeves, J.M., Darbeheshti, M., Baumgardner, D.G., Kok, G.L., Chung, S.H., Schulz, M., Hendricks, J., Lauer, A., Kärcher, B., Slowik, J.G., Rosenlof, K.H., Thompson, T.L., Langford, A.O., Loewenstein, M., and Aikin, K.C.: Single-particle measurements of midlatitude black carbon and light-scattering aerosols from the boundary layer to the lower stratosphere, J. Geophys. Res., 111, D16207, https://doi.org/10.1029/2006JD007076, 2006.

Seinfeld, J.H., Bretherton, C., Carslaw, K.S., Coe, H., DeMott, P.J. Dunlea, E.J., Feingold, G., Ghan, S., Guenther, A.B., Kahn, R., Kraucunas, I., Kreidenweis, S.M., Molina, M.J., Nenes, A., Penner, J.E., Prather, K.A., Ramanathan, V., Ramaswamy, V., Rasch, P.J., Ravishankara, A.R., Rosenfeld, D., Stephens, G., and Wood, R.: Improving our fundamental understanding of the role of aerosol−cloud interactions in the climate system. Proc. Natl. Acad. Sci. 113, 5781–5790, https://doi.org/10.1073/pnas.1514043113, 2016.

Springston, S., Koontz, A., and Trojanowski, R.: Ozone Monitor (AOSO3), Atmospheric Radiation Measurement (ARM) User Facility, https://doi.org/10.5439/1346692, Accessed Day Month Year, 2018.

Stein, A.F., Draxler, R.R., Rolph, G.D., Stunder, B.J.B., Cohen, M.D., and Ngan, F.: NOAA's HYSPLIT atmospheric transport and dispersion modeling system, Bull. Amer. Meteor. Soc., 96, 2059-2077, https://doi.org/10.1175/BAMS-D-14-00110.1, 2015.

Tilmes, S., Hodzic, A., Emmons, L.K., Mills, M.J., Gettelman, A., Kinnison, D.E., Park, M., Lamarque, J.-F., Vitt, F., Shrivastava, M., Campuzano Jost, P., Jimenez, J., and Liu, X.: Climate forcing and trends of organic aerosols in the Community Earth System Model (CESM2), J. Adv. Model Earth Sys., 11, 4323-4351, https://doi.org/10.1029/2019MS001827, 2019.

Tilmes, S., Emmons, L.K., Buchholz, R.R. and the CESM2 development team: CESM2.2/CAM-chem Output for Boundary Conditions. UCAR/NCAR - Atmospheric Chemistry Observations and Modeling Laboratory. Subset used Latitude: -50 to -10 S, Longitude: -90 to 40, Accessed 11 October 2023, https://doi.org/10.5065/XS0R-QE86, 2022.

Tomlinson, J.: Ultra high sensitivity aerosol spectrometer aboard aircraft (UHSAS-air), Atmospheric Radiation Measurement (ARM) User Facility, https://doi.org/10.5439/1524780, Accessed Day Month Year, 2018.

Twohy, C.H., Petters, M.D., Snider, J.R., Stevens, B., Tahnk, W., Wetzel, M., Russell, L., and Burnet, F.: Evaluationof the aerosol indirect effect in marine stratocumulus clouds: Droplet number, size, liquid water path, and radiative impact, J. Geophys.Res.,110, D08203, https://doi.org/10.1029/2004JD005116, 2005.

1113   Twomey, S.: Pollution and the planetary albedo, Atmos. Environ., 8, 1251–1256,
1114   https://doi.org/10.1016/0004-6981(74)90004-3, 1974.

1115   Uin, J., Senum, G., Koontz, A., Flynn, C., Salwen, C., and Hayes, C.: Ultra-High Sensitivity Aerosol
1116   Spectrometer (AOSUHSAS), Atmospheric Radiation Measurement (ARM) User Facility,
1117   https://doi.org/10.5439/1409033, Last accessed 15 April 2024, 2018.

1118   Varble, A., Nesbitt, S.W., Salio, P., Avila, E., Borque, P., DeMott, P., McFarquhar, G., van den Heever,
1119   S., Zipser, E., Gochis, D., Houze, R., Jensen, M., Kollias, P., Kreidenweis, S., Leung, R., Rasmussen, K.,
1120   Romps, D., and Williams, C.,: Cloud, Aerosol, and Complex Terrain Interactions (CACTI) field
1121   campaign report. Tech. Doc. DOE/SC-ARM-19-028, www.arm.gov/publications/programdocs/doe-sc-
1122   arm-19-028.pdf, 2019.

1123   Varble, A., Nesbitt, S.W., Salio, P., Hardin, J.C., Bharadwaj, N., Borque, P., DeMott, P., Feng, Z., Hill,
1124   T., Marquis, J., Matthews, A., Mei, F., Oktem, R., Castro, V., Goldberger, L., Hunzinger, A., Barry, K.,
1125   Kreidenweis, S., McFarquhar, G.M., McMurdie, L., Pekour, M., Powers, H., Romps, D.M., Saulo, C.,
1126   Schmid, B., Tomlinson, J., van den Heever, S., Zelenyuk, A., Zhang, Z., and Zipser, E., Utilizing a storm-
1127   generating hotspot to study convective cloud transitions: The CACTI experiment, Bull. Amer. Meteor.
1128   Soc., 102, E1597-E1620, https://doi.org/10.1175/BAMS-D-20-0030.1 2021.

1129   Varble, A.C., Igel, A.L., Morrison, H., Grabowski, W.W., and Lebo, Z.J.: Opinion: A critical evaluation
1130   of the evidence for aerosol invigoration of deep convection, Atmos. Chem. Phys., 23, 13791-13808,
1131   http://doi.org/10.5194/acp-23-13791-2023, 2023.

1132   Veals, P., Varble, A.C., Russell, J.O.H., Hardin, J.C., and Zipser, E.J.: A decrease in the depth of deep
1133   convective cores with increasing aerosol concentration during the CACTI campaign, J. Atmos. Sci., 79,
1134   705-722, https://doi.org/10.1175/JAS-D-21-0119.1, 2022.

1135   Wang Y., Ramesh, B.C., Giangrande, S.E., Fast, J., Gong, X., Zhang, J., Matthews, A., Mei, F., Odabasi,
1136   A.T., Shilling, J., Tomlinson, J., Wang, D., and Wang, J.: Examining the vertical heterogeneity of
1137   aerosols over the Southern Great Plains, Atmos. Chem. Phys., 23, 15671-15691.
1138   https://doi.org/10.5194/egusphere-2023-830, 2023.

1139   Watson-Parris, D., Schutgens, N., Reddington, C., Pringle, K.J., Liu, D., Allan, J.D., Coe, H., Carslaw,
1140   K.S., and Stier, P.: In situ constraints on the vertical distribution of global aerosol, Atmos. Chem. Phys.,
1141   19, 11765-11790, https://doi.org/10.5194/acp-19-11765-2019, 2019.

1142   Wiedinmyer, C., Kimura, Y., McDonald-Buller, E.C., Emmons, L.K., Buchholz, R.R., Tang, W., Seto,
1143   K., Joseph, M.B., Barsanti, K.C., Carlton, A.G., and Yokelson, R.: The fire inventory from NCAR
1144   version 2.5: An updated global fire emissions model for climate and chemistry applications, Geosci.
1145   Model Dev., 16, 3873–3891, https://doi.org/10.5194/gmd-16-3873-2023, 2023.

1146   Wofsy, S.C., Daube, B., Jimenez, R., Kort, E., Pittman, J.V., Park, S., Commane, R., Xiang, B., Santoni,
1147   G., Jacob, D., Fisher, J., Pickett-Heaps, C., Wang, H., Wecht, K.J., Wang, Q.-Q., Stephens, B.B., Shertz,
1148   S. Romashkin, P., Campos, T., Haggerty, J., Cooper, W.A., Rogers, D., Beaton, S., Hendershot, R.,
1149   Elkins, J.W., Fahey, D., Gao, R., Moore, F., Montzka, S.A., Schwarz, J., Hurst, D., Miller, B., Sweeney,
1150   C., Oltmans, S., Nance, D., Hintsa, E., Dutton, G., Watts, L., Spackman, R., Rosenlof, K., Ray, E.,
1151   Zondlo, M.A., Diao, M., Keeling, R., Bent, J., Atlas, E., Lueb, R., Mahoney, M.J., Chahine, M., Olson,
1152   E., Patra, P., Ishijima, K., Engelen, R., Flemming, J., Nassar, R., Jones, D.B.A., and Fletcher, S.E.M.:
1153   HIAPER Pole-to-Pole Observations (HIPPO): Fine-grained, global scale measurements of climatically
1154   important atmospheric gases and aerosols, Philos. Trans. Royal Soc., 369, 2073-2086,
1155   DOI:10.1098/rsta.2010.0313, 2011.

1156   Wood, R., Mechoso, C.R., Bretherton, C.S., Weller, R.A., Huebert, B., Straneo, F., Albrecht, B.A., Coe,
1157   H., Allen, G., Vaughan, G., Daum, P., Fairall, C., Chand, D., Gallardo Klenner, L., Garreaud, R., Grados,
1158   C., Covert, D.S., Bates, T.S., Krejci, R., Russell, L.M., de Szoeke, S., Brewer, A., Yuter, S.E., Springston,

1159   S.R., Chaigneau, A., Toniazzo, T., Minnis, P., Palikonda, R., Abel, S.J., Brown, W.O.J., Williams, S.,
1160   Fochesatto, J., Brioude, J., and Bower, K.N.: The VAMOS Ocean-Cloud-Atmosphere-Land Study
1161   Regional Experiment (VOCALS-REx): Goals, platforms, and field operations, Atmos. Chem. Phys., 11,
1162   627-654. https://doi.org/10.5194/acp-11-627-2011, 2011.

1163   Zawadowicz, M., Watson, T., Hayes, C., Allain, M., Salwen, C., and Behrens, B.: Aerosol Chemical
1164   Speciation Monitor (AOSACSM), Atmospheric Radiation Measurement (ARM) User Facility,
1165   https://doi.org/10.5439/1558768, Last accessed 15 April 2024, 2018.

1166   Zelenyuk, A., Berg, L.K., Wilson, J., Zhang, Z., Wang, J., and Mueller, K., Airborne single particle mass
1167   spectrometers (SPLAT II & miniSPLAT) and new software for data visualization and analysis in a geo-
1168   spatial context, J. Amer. Soc. Mass Spectrom., 26, 257–270, https://doi.org/10.1007/s13361-014-1043-4,
1169   2015.

1170   Zhang, Z., Varble, A.C., Feng, Z., Hardin, J., and Zipser, E.: Growth of mesoscale convective systems in
1171   observation and a seasonal convection-permitting simulation over Argentina, Mon. Wea. Rev., 149, 3469-
1172   3490, https://doi.org/10.1175/MWR-D-20-0411.1, 2021.

1173